J. Fluid Mech. (2004), *vol.* 521, *pp.* 69–104.
DOI: 10.1017/S0022112004000965 Printed in the United Kingdom

On gravity currents propagating at the base of a stratified ambient: effects of geometrical constraints and rotation

By MARIUS UNGARISH[1] AND HERBERT E. HUPPERT[2]

[1]Department of Computer Science, Technion, Haifa 32000, Israel

[2]Institute of Theoretical Geophysics, Department of Applied Mathematics and Theoretical Physics, University of Cambridge, Wilberforce Road, Cambridge CB3 0WA, UK

(Received 28 August 2003 and in revised form 26 May 2004)

The behaviour of an inviscid gravity current released from a lock and propagating over a horizontal boundary at the base of a stratified ambient fluid is considered in the framework of a one-layer shallow-water formulation. Solutions for two-dimensional rectangular and axisymmetric geometries, with emphasis on the rotation of the latter, were obtained by a Lax–Wendroff scheme. Box-model approximations are also discussed. The axisymmetric and rotating case admits steady-state lens structures, for which approximate and numerical solutions are presented. In general, the stratification reduces the velocity of propagation and enhances the Coriolis effects in a rotating system (in particular, the maximal radius of propagation decreases). Comparisons of the shallow-water results with Navier–Stokes simulations and laboratory experiments indicate good agreement, at least for the initial period of propagation. The major deficiency of this shallow-water model is the lack of incorporation of internal waves. In particular, if the propagation is at subcritical speed, the applicability of the model is restricted to the time prior to the first effective interaction between the head of the gravity current and the lowest-order internal wave; an estimate of this position is presented.

1. Introduction

The study of gravity currents, which occur whenever fluid of one density flows primarily horizontally into fluid of a different density, has a long history (Simpson 1997; Huppert 2000). Part of the motivation for these investigations is that gravity currents arise frequently in both industrial and natural settings. A gravity current may be driven by compositional or temperature differences, leading to a homogeneous current, or by suspended particulate matter, leading to a particle-driven current (Bonnecaze *et al.* 1993, 1995; Huppert 1998). Combinations of both particle and compositional or temperature differences can also occur, as discussed by Hogg, Hallworth & Huppert (1999). Currents may propagate in a variety of geometries, including a rectangular two-dimensional situation or a cylindrical axisymmetric configuration. They may also be influenced by sidewalls and/or topographic constraints. Many of these processes have now been investigated. A typical study considers the instantaneous release of a constant volume of heavy fluid from behind a lock into a large reservoir of a less dense *homogeneous* fluid above an impermeable horizontal boundary. In this paper, our primary aim is to evaluate theoretically the effects of a stratified ambient on the propagation of high-Reynolds-number currents resulting from the instantaneous release of a finite volume of fluid of constant density. We consider both rectangular two-dimensional and axially symmetric cylindrical geometries. Background rotation in the latter, which contributes significant Coriolis-centrifugal effects, is also considered. Our work may find applications in areas such as the intrusion of fronts in both the oceans and atmosphere and is also relevant to environmental control and hazard assessment.

A study of the prototype problem has been presented by Maxworthy *et al.* (2002). They considered the propagation of a saline current released from behind a lock over a horizontal bottom into a linearly stratified saline ambient in a rectangular container whose upper boundary was open to the atmosphere. The investigation was a combination of laboratory and numerical experiments. The numerical solutions, obtained from the full Boussinesq formulations, were in very good agreement with the measurements. Attention was focused on the influence of the stratification on the speed of propagation of the nose.

In Ungarish & Huppert (2002, referred to hereinafter as UH), we developed the theoretical interpretation of the experimental observations in the framework of a shallow-water (SW) theory. The analysis indicated that the effects of stratification can be incorporated into the classical homogeneous-fluid SW formulation by: (i) a modified pressure gradient correlation in the horizontal momentum equation; and (ii) a modified pressure head correlation in the boundary condition which specifies the speed of propagation of the front (nose). These modifications introduce a dimensionless parameter, S, which expresses the relative strength of the stratification compared to the density difference between the current and the top of the ambient. The parameter as defined varies from $S=0$ for the homogeneous case to $S=1$ when the density of the ambient at the bottom is equal to that of the current. The analysis of UH did not solve the SW partial differential equations for the general case; they were concerned only with the velocity of propagation in the initial slumping stage, during which the nose propagates with constant velocity and height (for rectangular geometry only). For this case, the solution can be reduced to simple, mainly analytical, calculations. The results for the velocity of propagation were in good agreement with the corresponding experimental measurements of Maxworthy *et al.* (2002), and also with numerical solutions of the Navier–Stokes equations developed in UH.

These encouraging results motivated this extension. The objectives are to investigate additional features of the propagation of gravity currents into a stratified ambient fluid, with the aid of the previously developed theoretical formulations. In particular, we now relax the restriction of our investigation beyond the slumping stage in a two-dimensional geometry with its constant velocity of propagation of the front and describable by analytical solutions of the SW equations. We employ a numerical finite-difference code to solve the SW equations in the more general circumstances, with the objectives of: (i) following the propagation of a rectangular current for a longer time and distance than in previous papers; and, in particular, (ii) solving for axisymmetric currents, mostly when subject to effects of rotation (i.e. Coriolis-centrifugal forces due to the rotation of the system). The rotating configuration also includes the quasi-steady-state lens structure for which we shall derive results from the SW theory. The initial time-dependent propagation usually overshoots the radius of the lens. The details of this effect (connected with the important Rossby adjustment process) have not been investigated for the stratified ambient. A related problem, of homogeneous lenses in a stratified rotating fluid, has been considered before both theoretically and experimentally by Gill (1981), Griffiths & Linden (1981) and Hedstrom & Armi (1988), but the generating process they considered was a slow

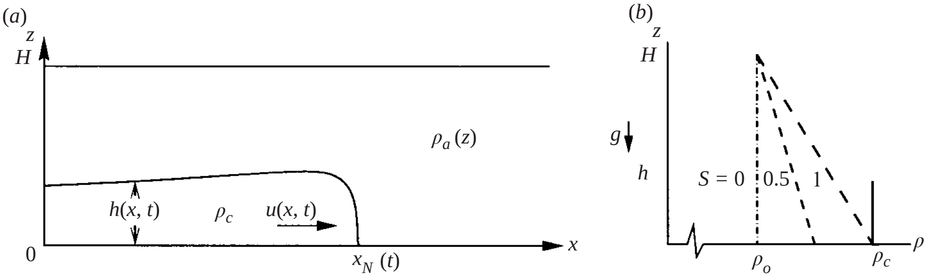

FIGURE 1. Schematic description of the system: (*a*) the geometry; and (*b*) the density profiles in the current (solid line) and ambient, for various values of S (dashed lines).

intrusion, not an instantaneous release from behind a lock of a gravity current of constant volume, as discussed in § 3.1.

The elementary system under consideration is sketched in figure 1. A deep layer of ambient fluid, of density $\rho_a(z)$, lies above a horizontal surface at $z = 0$. Gravity acts in the $-z$-direction. In the rectangular case, the system is bounded by parallel vertical smooth impermeable surfaces and the current propagates in the direction labelled x. At time $t = 0$, a given volume of homogeneous fluid of density $\rho_c \geqslant \rho_a(z = 0) \equiv \rho_b$ and kinematic viscosity ν, initially at rest in a rectangular box of height h_0 and length x_0, is instantaneously released into the ambient fluid. A two-dimensional current begins to spread. We assume that the appropriate Reynolds number of the horizontal flow is large and hence viscous effects can be neglected.

In the axially symmetric geometry, the coordinate x is replaced by the cylindrical radial coordinate r, and the dense fluid is initially stored in a cylinder of radius r_0 and height h_0. The entire system is assumed to be rotating with constant angular velocity Ω about the z-axis. In this case, the motion is affected by the Coriolis-centrifugal forces, and the usual propagation of the dense fluid in the radial direction is coupled with its motion in the azimuthal direction. An additional dimensionless parameter enters the formulation, $\mathscr{C}$, which represents the ratio of Coriolis to inertia forces. The case of a homogeneous ambient has been discussed by Ungarish & Huppert (1998), Hallworth, Huppert & Ungarish (2001) and Ungarish & Zemach (2003); significant features are the finite radius of propagation and the possibility of steady-state lens structures. We are interested in small values of $\mathscr{C}$; otherwise, the Coriolis effects restrict the propagation to a small distance and no real gravity current develops.

The major deficiency of the one-layer SW model used in this work is that internal gravity waves are discarded. Our arguments are that these waves have little influence on the motion of the current in certain practical circumstances, at least during a significant initial period of propagation, and that, for analytical progress, it is worthwhile, perhaps even necessary, to decouple the current and the waves. A closely related problem is the stratified flow over a fixed obstacle, a topic covered thoroughly by Baines (1995), from which useful insights can be gained. However, the gravity current is a time-dependent deformable 'obstacle', whose shape interacts with the waves it produces in the ambient. The analytical study of this flow field is evidently a formidable task, and our idea is to attempt the following decoupling: first, solve for the propagation of the gravity current under the assumption of an unperturbed ambient; next, consider the perturbations produced in an impulsively started flow over an obstacle of prescribed height $h(x, t)$ over the bottom (the relative velocity far upstream is that of the front of the current, $u_N(t)$). In this paper, we solve only the first problem, which is the easier, and yet the more fundamental one, as reflected by the accurate predictions provided by the SW results for a considerable time interval. We note in passing that the waves are intrinsically incorporated in the Navier–Stokes simulations performed in our study.

The structure of the paper is as follows. In § 2, the model equations of motion, based on shallow-water approximations and the appropriate boundary conditions, are developed, and the method of solution is briefly discussed. Results for the rectangular case are presented and compared with the experiments of Maxworthy *et al.* (2002) and numerical solutions of the Navier–Stokes equations. The extensions of the SW theory to the axially symmetric case, with and without rotation (including the steady-lens limit), are developed in § 3. Here, comparisons with numerical solutions of the Navier–Stokes equations and to recent unpublished experiments are presented. Next, in § 4, box model approximations are briefly discussed. We present a summary of our results and some concluding remarks in § 5. The Appendix contains a short description of the Navier–Stokes numerical simulation used in this work.

2. Rectangular two-dimensional case

The configuration is sketched in figure 1. For the rectangular case, we use an $\{x, y, z\}$ Cartesian coordinate system with corresponding $\{u, v, w\}$ velocity components, and assume that the flow does not depend on the coordinate y and that $v \equiv 0$.

The formulation has been presented in UH. For the sake of completeness we briefly repeat here only some essentials.

Initially, the height of the fluid which will make up the propagating current is h_0, its length x_0 and the density ρ_c. The height of the ambient fluid is H and the density in this domain decreases linearly with z from ρ_b to ρ_o, where the subscripts b, o refer to bottom and open surface values, respectively. (Note that the linear variation is taken here for simplicity of analysis, but is not essential.)

It is convenient to use ρ_o as the reference density and to introduce the reduced density differences and ratios between them

$$\epsilon = \frac{\rho_c - \rho_o}{\rho_o}, \quad \epsilon_b = \frac{\rho_b - \rho_o}{\rho_o}, \tag{2.1}$$

and

$$S = \epsilon_b/\epsilon, \tag{2.2}$$

from which it follows that

$$\rho_c = \rho_o(1+\epsilon), \quad \rho_a = \rho_o\left[1 + \epsilon S\left(1 - \frac{z}{H}\right)\right]. \tag{2.3}$$

The parameter S represents the magnitude of the stratification in the ambient fluid, and we consider only $0 \leqslant S \leqslant 1$. The homogeneous ambient is recovered by setting $S = 0$. We also define the reference reduced gravity,

$$g' = \epsilon g, \tag{2.4}$$

where g is the acceleration due to gravity.

We recall that the leading, or mode one, linear internal waves in a closed two-dimensional channel propagate with velocity

$$u_W = \pm\frac{\mathscr{N} H}{\pi}, \tag{2.5}$$

where $\mathscr{N}=(Sg'/H)^{1/2}$ is the buoyancy frequency (Baines 1995); we emphasize that here the variables are in dimensional form.

2.1. *SW formulation*

We use a one-layer approximation which is expected to capture many of the important features of the flow, and is the simplest shallow-water model. In the ambient-fluid domain we assume that $u = v = w = 0$ and hence the fluid is in purely hydrostatic balance and maintains the initial density $\rho_a(z)$. The motion is assumed to take place in the lower layer only, $0 \leqslant x \leqslant x_N(t)$ and $0 \leqslant z \leqslant h(x,t)$. As in the classical inviscid shallow-water analysis of a gravity current in a homogeneous ambient, we argue that the predominant vertical momentum balance in the current is hydrostatic and that viscous effects in the horizontal momentum balance are negligibly small. Hence, the motion is governed by the balance between pressure and inertia forces in this horizontal direction.

A relationship between the pressure fields and the height $h(x,t)$ is now obtained. In the motionless ambient fluid, which is open to the atmosphere, the pressure does not depend on x. The hydrostatic balances are $\partial p_i/\partial z = -\rho_i g$, where $i = a$ or c. Use of (2.3) then yields

$$p_a(z,t) = -\rho_o\left[1+\epsilon S\left(1-\frac{1}{2}\frac{z}{H}\right)\right]gz + C \tag{2.6}$$

and

$$p_c(x,z,t) = -\rho_o(1+\epsilon)gz + f(x,t), \tag{2.7}$$

where the constant C reflects the fact that a constant pressure is assumed at the top of the ambient at $z = H$ (the deformation of the free surface is negligible for $\epsilon \ll 1$). Pressure continuity between the ambient and the current on the interface $z = h(x,t)$ determines the function $f(x,t)$ of (2.7) and we obtain, after some algebra,

$$\frac{\partial p_c}{\partial x} = \rho_o g'\frac{\partial h}{\partial x}\left[1 - S\left(1-\frac{h}{H}\right)\right]. \tag{2.8}$$

As expected, the effect of stratification on the gravity current, as reflected by the horizontal pressure gradient, increases as S increases. However, we must keep in mind that internal waves should be expected to develop in the stratified ambient owing to the propagation of the current (in a frame attached to the nose, this resembles the motion over an obstacle, see for example Baines 1995). These waves may disturb the ideal hydrostatic upper-ambient-layer assumption, at least in some parameter range. This will be verified and discussed later.

The next step is to consider the vertical average of the horizontal inviscid momentum equation in the dense fluid, and eliminate the pressure term by (2.8). In conjunction with volume continuity, we obtain a system of equations for $h(x,t)$ and for the averaged longitudinal velocity, $u(x,t)$.

It is convenient to scale the dimensional variables (denoted here by asterisks) by

$$\{x^*, z^*, h^*, H^*, t^*, u^*\} = \{x_0 x, h_0 z, h_0 h, h_0 H, Tt, Uu\}, \tag{2.9}$$

with

$$U = (h_0 g')^{1/2} = \mathscr{N}\sqrt{\frac{H}{S}}h_0, \quad T = x_0/U, \tag{2.10}$$

where U is a typical inertial velocity of propagation of the nose of the current and T is a typical time period for longitudinal propagation for a typical distance x_0; we emphasize that $\mathscr{N}$ is dimensional. Note that the horizontal and vertical lengths are scaled differently, which, as pointed out by Ungarish & Huppert (1999), removes the initial aspect ratio h_0/x_0 from the SW analysis in the homogeneous circumstances, and this applies also to the stratified case considered here. However, we shall see that the parameter h_0/x_0 enters the present problem at a later stage, in the context of wave–current interaction. We note in passing that the dimensionless velocity of the leading waves, u_W, see (2.5), is $\pm(SH)^{1/2}/\pi$.

Hereinafter, dimensionless variables are used, unless stated otherwise. In any case, x_0, h_0 and $\mathscr{N}$ are dimensional.

In conservation form, the equations can be written as

$$\frac{\partial h}{\partial t} + \frac{\partial}{\partial x}(uh) = 0, \tag{2.11}$$

and

$$\frac{\partial}{\partial t}(uh) + \frac{\partial}{\partial x}\left[u^2 h + \tfrac{1}{2}(1-S)h^2 + \tfrac{1}{3}S\frac{h^3}{H}\right] = 0. \tag{2.12}$$

In characteristic form, these become

$$\begin{bmatrix} h_t \\ u_t \end{bmatrix} + \begin{bmatrix} u & h \\ 1 - S + S\dfrac{h}{H} & u \end{bmatrix} \begin{bmatrix} h_x \\ u_x \end{bmatrix} = \begin{bmatrix} 0 \\ 0 \end{bmatrix}. \tag{2.13}$$

The characteristic curves and relationships provide useful information for the solution of the system, including a proper requirement of boundary conditions for the interface height h at the ends of the current domain. Following the standard procedure, we obtain

$$a(h)\,\mathrm{d}h \pm \mathrm{d}u = 0, \tag{2.14}$$

where

$$a(h) = \left[\frac{1 - S + (Sh)/H}{h}\right]^{1/2}, \tag{2.15}$$

on the characteristics with $\mathrm{d}x/\mathrm{d}t = c_{\pm}$, where

$$c_{\pm} = u \pm \left[h\left(1 - S + S\frac{h}{H}\right)\right]^{1/2}. \tag{2.16}$$

The initial conditions are zero velocity and unit dimensionless height and length at $t = 0$. Also, the velocity at $x = 0$ is zero, and an additional condition is required at the nose $x = x_N(t)$.

We use the conditions which have been developed and verified in UH, based on the arguments that, briefly: (i) the velocity of the nose is proportional to the square-root of the pressure head (per unit mass); (ii) the factor of proportionality, defined as the Froude number Fr, varies in a quite narrow range with the ratio h_N/H; and (iii) the behaviour of Fr in the stratified case is approximated well by the well-known homogeneous situation. Consequently,

$$u_N = Fr\, h_N^{1/2} \times \left[1 - S\left(1 - \frac{1}{2}\frac{h_N}{H}\right)\right]^{1/2}. \tag{2.17}$$

The term in the square brackets of (2.17) is equal to 1 in the non-stratified case ($S = 0$), and smaller than 1 for $S > 0$. This term expresses the explicit slow-down of the head owing to the stratification effects.

The value of Fr is required to close the SW formulation. The consensus is that a quasi-steady motion of the head can be assumed for which the steady-state considerations of Benjamin (1968) predict that Fr is a function of h_N/H (Klemp, Rotunno & Skamarock 1994). The theoretical value is slightly higher than observed in real currents, and corrections have been suggested. In this spirit, we shall use the simple empirical correlation derived by Huppert & Simpson (1980)

$$Fr(h_N/H) = \begin{cases} 1.19 & (0 \leqslant h_N/H \leqslant 0.075), \\ 0.5H^{1/3}h_N^{-1/3} & (0.075 \leqslant h_N/H \leqslant 1). \end{cases} \tag{2.18}$$

It was shown in UH that the combination (2.17)–(2.18) provides complete qualitative agreement and very good quantitative agreement with the experimental results of Maxworthy *et al.* (2002) for the nose velocity during the slumping stage, which justifies its use in the present study.

2.2. *Results and comparisons for two-dimensional cases*

Analytical results of the foregoing SW formulation may be obtained for restricted circumstances. UH obtained the initial slumping velocity of the nose, u_N, in a two-dimensional geometry, by integrating the balance on the forward characteristic from the unperturbed bulk of dense fluid to the point where it intersects with the nose condition. The analytical behaviour of $h(x, t)$ and $u(x, t)$ in the 'dam-break' stage was presented by Ungarish (2004). However, in general, the resulting SW system requires numerical solution. This is the situation also for the classical homogeneous case. The present formulation includes a new physical effect, the stratification of the ambient, reproduced by the additional dimensionless parameter S. However, this does not affect the qualitative properties of the SW system as known from the classical case (recovered here for $S = 0$). For the range of interest, $0 \leqslant S \leqslant 1$, the resulting system is hyperbolic and well posed. The characteristics are real-valued and propagate faster than the fluid near the boundaries. We therefore used the robust two-step Lax–Wendroff finite-difference method (Morton & Mayers 1994; Press *et al.* 1992) to integrate the SW equations of motion. This scheme has been used successfully before in the solution of various gravity currents (Bonnecaze *et al.* 1993; Ungarish & Huppert 1998) and we found that, after the modification introduced by the stratification, it also works efficiently in the cases considered in this paper (two-dimensional and axisymmetric with and without rotation). The current domain $[0, r_N(t)]$ is mapped into a constant [0, 1] domain, which is discretized in equal intervals. The typical grid has 100 points, with time step 0.8×10^{-2}, and the run time is insignificant.

The validity of the results may be affected by the neglected effect of the internal gravity waves. We claim that in the present initial-value problem this effect influences the propagation of subcritical currents only. An inspection of (2.17) indicates that the type of current depends on the values of H and S. Since Fr is about 1 and h_N smaller than 1 (typically, 0.5 in the initial stages of motion), (2.17) indicates that u_N is smaller then 1 and decreases with S, while, on the other hand, the forward wave speed $u_W = (SH)^{1/2}/\pi$ increases with S and can attain values both smaller and larger than 1. Consequently, both supercritical ($u_N > u_W$) and subcritical ($u_N < u_W$) currents are feasible; the former are expected for weak stratification and shallow ambients (small S and not large H) and the latter for strong stratification and/or deep ambients (S close to 1 and/or large H). The critical curve $S_{cr}(H)$ obtained from our formulation

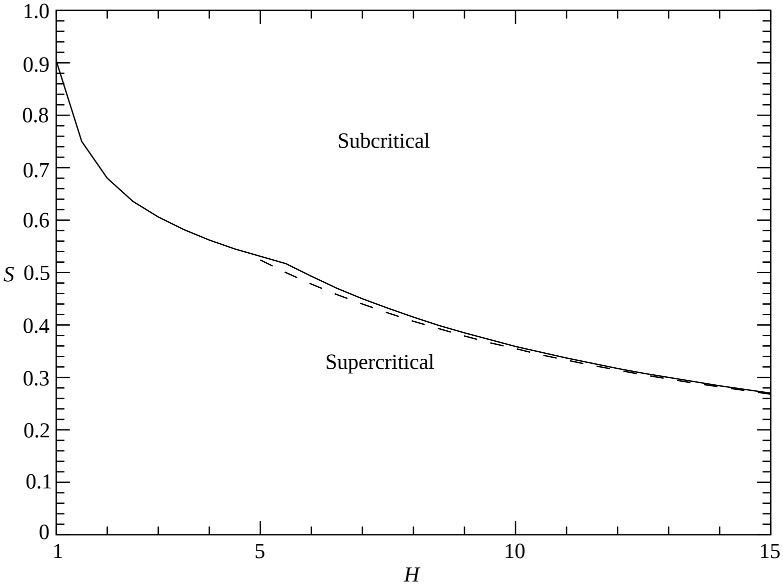

FIGURE 2. The sub- and supercritical subdomains in the (S,H)-domain, as predicted by the SW theory. The dashed line is the approximation S_{cr} for large H.

(using the initial slumping velocity u_N derived in UH) is displayed in figure 2. An expansion for large H yields the approximation

$$S_{cr} = \left[1 + \left(\frac{Fr(0)+2}{2\pi Fr(0)}\right)^2 H\right]^{-1}, \tag{2.19}$$

and in the present case $Fr(0)=1.19$, see (2.18). The conclusion is that a significant portion of the, (S,H)-domain corresponds to supercritical currents, and for these circumstances the wave-propagation interaction is expected to be unimportant for at least the SW slumping distance, $x_N \approx 3$ (eventually the velocity of the front decays and the subcritical domain is attained, but viscous effects may also become important at this stage).

On the other hand, even for a subcritical current, the initial motion is dominated by the inertia–pressure balance in the dense fluid, not by the waves in the ambient. This has been clearly observed in the experiments of Maxworthy *et al.* (2002). Using the insights provided by these experiments, we can estimate the position x_2 where the first strong interaction between the waves and the nose occurs as follows. First, the nose propagates two wavelengths with the wave locked to the head. Next, the wave is unlocked from the head and moves forward relative to the current until the crest reaches the nose (and thus slows it down). No mixing or instabilities were observed during this process. The analogy with the obstacle problem Baines (1995) indicates that the wavelength (scaled with x_0) is $\lambda = 2\pi(H/S)^{1/2}(h_0/x_0)u_N$. The propagation with velocity u_N of the tandem motion over 2 λ plus the relative motion (with velocity $u_W - u_N$) over $\lambda/4$ yields

$$x_2 = 1 + 2\frac{h_0}{x_0}H\left(\frac{\pi u_N}{\sqrt{SH}}\right)\left[2 + \frac{0.25}{\left(\dfrac{\pi u_N}{\sqrt{SH}}\right)^{-1} - 1}\right]. \tag{2.20}$$

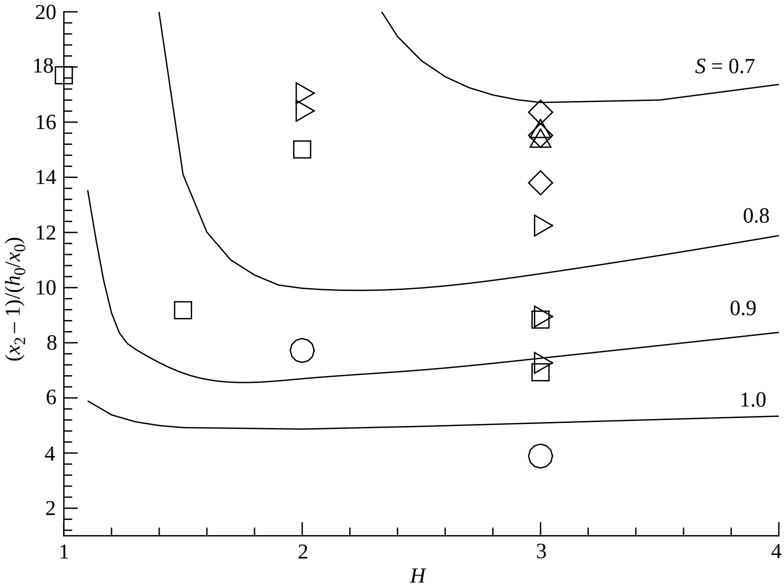

FIGURE 3. The distance of propagation where wave–nose interaction becomes important for subcritical currents, as a function of H for various S. The lines show the present SW estimate, the points are from Exp. 1, 4, 8–12, 15–16, 19, 21–25, 28, 29, 32 of Maxworthy *et al.* The symbols circle, square, right triangle, diamond and delta correspond to $S \approx 1.0, 0.90, 0.80, 0.70$ and 0.6, respectively.

Using again our results for the initial u_N as a function of S and H we obtain straightforward estimates of x_2.

Maxworthy *et al.* (2002) provided the experimental distance (from the gate of the lock) X_{tr} where significant deceleration of the nose occurs. A comparison with the present result, for subcritical currents, is shown in figure 3. There is some scatter of the experimental points, but overall the magnitude and the trend predicted by (2.20) are confirmed. (In view of the simplification involved in the derivation of (2.20), and keeping in mind that the practical detection of x_2 is not a clear-cut task, a closer agreement could not be expected.) Thus, we think that (2.20) captures well the parameters that govern the start of interactions between the waves and the propagation of the subcritical current, and can be used as a reliable estimate of the range of applicability of the SW results. The behaviour of x_2 (see figure 3) indicates that there are many significant combinations of S, H and h_0/x_0 for which the present SW results are relevant to subcritical currents. Eventually, the effects of the waves become dominant and the presently discussed density-driven propagation will evolve into a wave-dominated flow field; this complex transition, as elucidated by Manasseh, Ching & Fernando (1998) (where other important references are also given) requires a different type of investigation and is left for future work.

We now proceed to a more detailed solution of two typical cases.

Consider the case corresponding to ‘Run 5’ of Maxworthy *et al.* (2002): $H = 3$ and $S = 0.293$. (Here, $U = 23.82\,\mathrm{cm\,s^{-1}}$, $T = 0.840\,\mathrm{s}$, $h_0 = 5\,\mathrm{cm}$, $x_0 = 20\,\mathrm{cm}$, $\epsilon = 0.1156$, $\mathscr{N} = 1.48\,\mathrm{s^{-1}}$). The calculated SW profiles of h and u as functions of x at various times are shown in figure 4.

Maxworthy *et al.* (2002) consider this configuration as typical to the supercritical domain, and emphasize that in this case no wave generation behind the head and

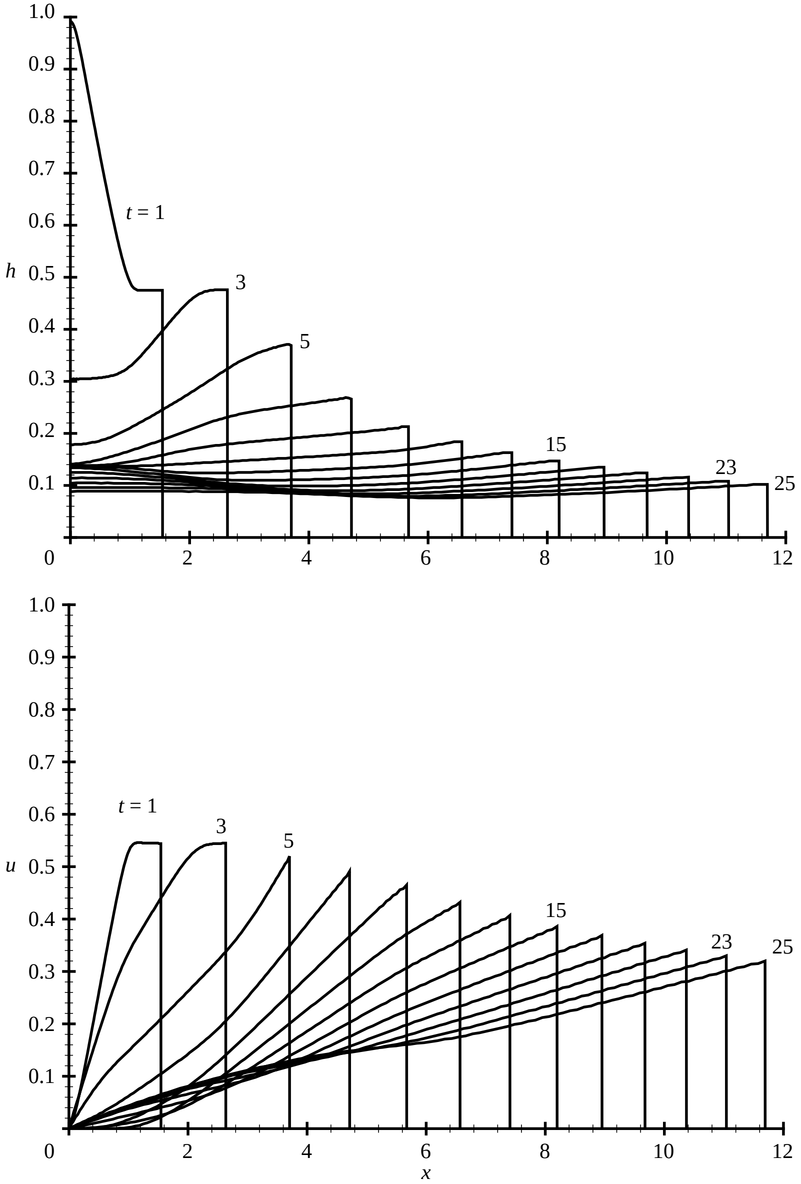

Figure 4. SW predicted profiles for Run 5 at $t = 1(2)25$.

no wave–head interaction is observed (at least during the initial propagation). This is in agreement with our domain diagram given in figure 2. To be specific, the initial velocity of propagation predicted by SW, $u_N = 0.54$, is larger than $u_W = 0.30$.

Figure 5 presents a comparison between the experimental results (taken from figure 5 of Maxworthy *et al.*) and SW predictions for x_N as a function of t. The agreement is excellent for $t < 10$, and afterwards the experimental results lag slightly behind the SW results. Overall, the agreement is satisfactory and the discrepancy at the later stage can be attributed to viscous and mixing effects which are not incorporated in the SW model. (The graph of x_N *vs.* t displays some weak oscillations after $t = 10$,

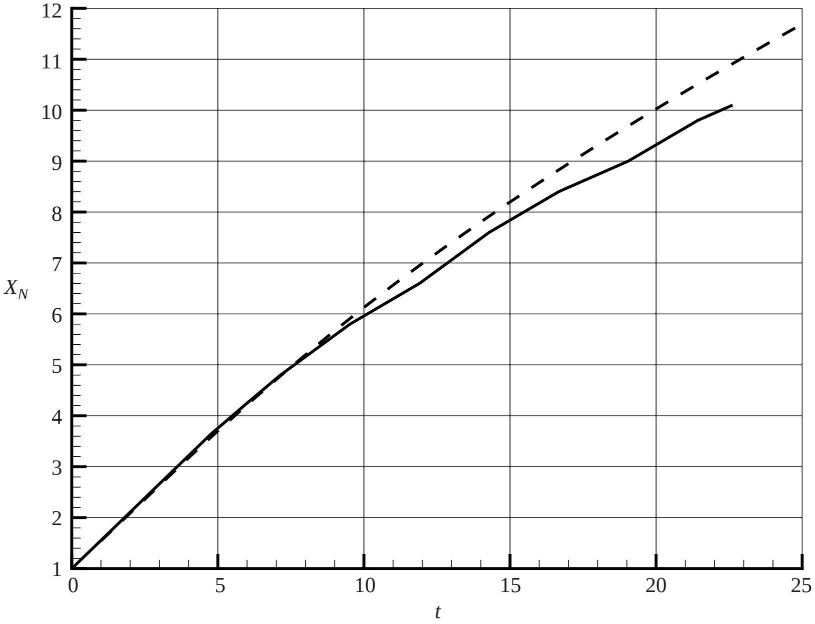

FIGURE 5. Comparisons of experiment (full line) and SW (dashed line) results for Run 5 of Maxworthy *et al.* (2002).

which may be the result of internal waves in the ambient or of measurement errors, but their amplitude and mean contribution to the main propagation are insignificant.)

A typical subcritical gravity current is illustrated in Maxworthy *et al.* (2002) by experiment 'Run 19', with $H=3$ and $S=0.72$. (Here $U=19.86\,\mathrm{cm\,s^{-1}}$, $T=1.01\,\mathrm{s}$, $h_0=5\,\mathrm{cm}$, $x_0=20\,\mathrm{cm}$, $\epsilon=0.0804$, $\mathscr{N}=1.94\,\mathrm{s^{-1}}$). The experimentally detected subcritical type of current is in agreement with our domain diagram given in figure 2. To be specific, in this case the initial velocity of propagation predicted by SW, $u_N=0.38$, is smaller than $u_W=0.47$. The SW profiles of h and u as functions of x at various times are shown in figure 6; the qualitative behaviour is similar to that of Run 5, figure 4, but the velocity is smaller in the present case for which S is larger. Comparisons for the propagation as a function of time are presented in figure 7. We observe that, initially, there is excellent agreement between SW predictions and experiment. However, at $x\approx 5$, the propagation of the real current is strongly hindered by the interaction between the nose and the waves. For the combination $S=0.72$, $H=3$ and $h_0/x_0=0.25$ used in the experiment, the theoretical start of interaction, see (2.20), is at $x_2=4.8$ (it is remarkable that the corresponding reported experimental value X_{tr} yields, in our scaling, the same result).

The interaction extends about 5 dimensionless time units, after which the previous speed is recovered. The SW solution evidently misses this interaction; the SW curve shows no special behaviour in the pertinent time period, and, consequently, a significant discrepancy of x_N is present for $t>15$.

To further corroborate our predictive tools we also performed numerical computations of the Navier–Stokes (NS) equations. Details of our finite-difference numerical code are presented the Appendix. We used a mesh of 320 horizontal and 200 vertical intervals. The dimensionless length of the tank, x_w, was 8, sufficiently large to avoid the influence of the reflected wave on the motion of the current. In contrast to the

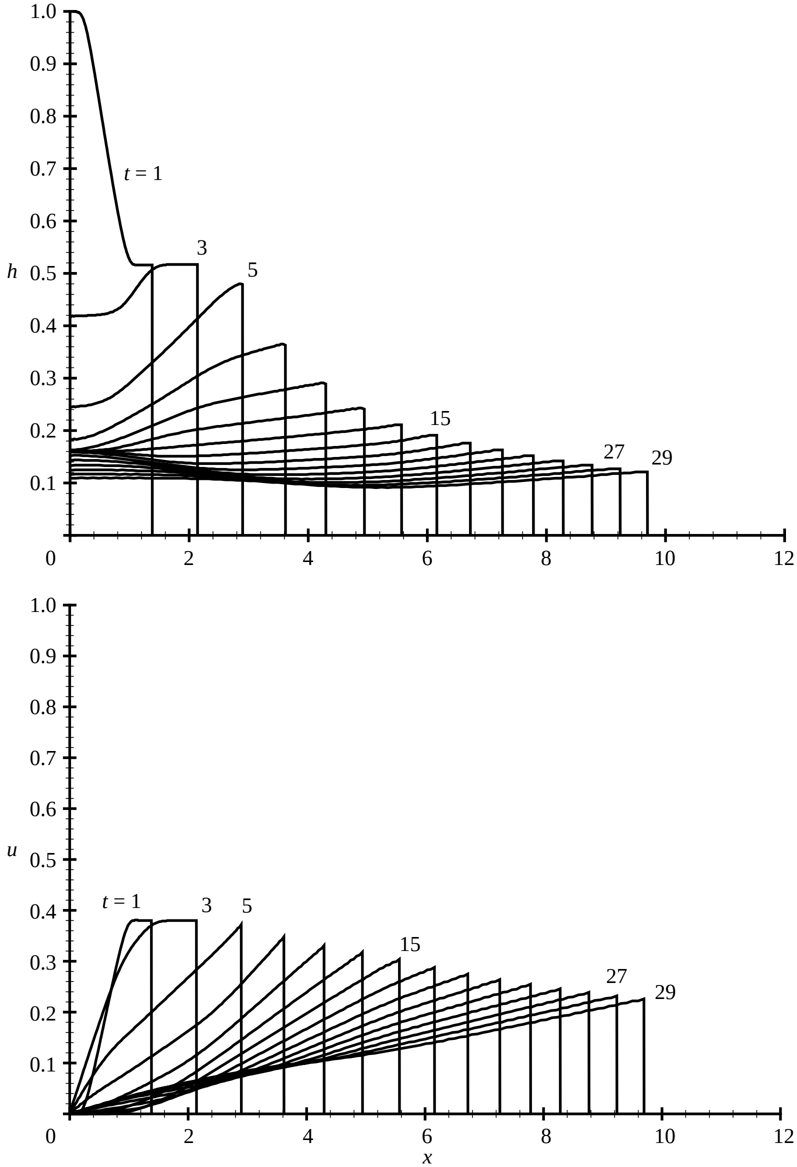

FIGURE 6. SW predicted profiles for Run 19 at $t = 1(2)29$.

SW solution, the NS computations require many CPU hours on powerful computers. The comparison of the NS value of x_N as a function of t with experimental and SW results is presented in figure 7. The three results are in excellent agreement for $t < 12$. Afterwards, some strong deceleration of the nose occurs in the NS results, in perfect agreement with the experiment, but with no counterpart in the SW solution. This strengthens the reliability of the NS code and also indicates that the interaction between the waves and the head is a robust property of the system, that occurs after a certain interval of propagation during which the SW approximation can be applied. Indeed, the NS results display pronounced oscillations of the isopycnals in the region

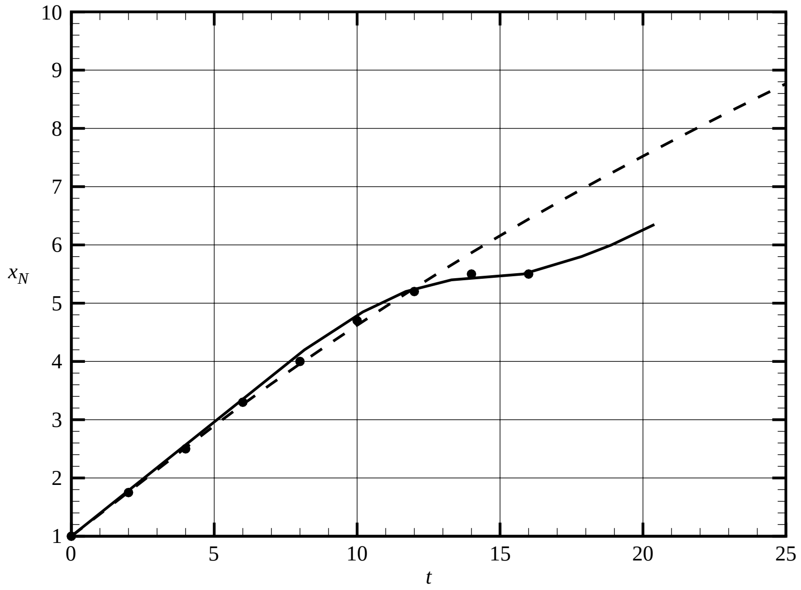

FIGURE 7. Comparisons of experiment (full line), SW (dashed line) and numerical Navier–Stokes (symbols) results for Run 19 of Maxworthy *et al.* (2002).

of the nose, figure 8, which confirm the experimentally derived connection of the wave–nose interaction hindrance.

The internal stratification waves are, as anticipated, an important ingredient in the motion of the subcritical gravity current after some initial time. The numerical NS simulation predict well the time and the nature of the wave–current interaction. However, the present SW model, which ignores these waves, predicts accurately the motion for a limited interval only. This is consistent with our attempt to decouple the problems of current (assuming an unperturbed ambient) and waves. Here we solve only the first problem, which is the easier, and yet the more fundamental one, as reflected by the accurate predictions provided by the foregoing SW results for a considerable time interval.

The wave problem that must be subsequently treated is expected to resemble the 'small amplitude topography' analysis (Baines 1995 § 5.2), at least when H/S is large. The dominant $\mathcal{N}h/U$ parameter of the obstacle can be expressed in our case as $(S/H)^{1/2}(h_N/u_N)$, and the typical wavelength, scaled with x_0, is $\lambda = 2\pi(H/S)^{1/2}(h_0/x_0)u_N$ (consistent with the observation of Maxworthy *et al.* 2002 figure 14 for the subcritical regime). During the slumping stage, (h_N/u_N) and u_N are constant, thereafter both decrease with time. At the beginning of the motion the 'obstacle' encountered by the ambient is the protruding rectangle of length $a = u_N t$ (the domain behind the lock $x < 1$ undergoes a gentle depression over a similar length) and hence $\lambda/a = 2\pi(H/S)^{1/2}(h_0/x_0)/t$ is large for some time interval, during which the buoyancy reaction to the obstacle is expected to be quite mild. The inherent time-dependent shape of the current renders the steady-state features of the classical investigations of the stratified flow over a fixed obstacle, and in particular Long's model results, of limited relevance to the times of propagation discussed here. Intriguing questions about upstream disturbances and columnar modes cannot yet be answered.

In summary, we showed that the present SW theory provides a reliable means for determining *a priori* the super- or subcritical classification of a gravity current

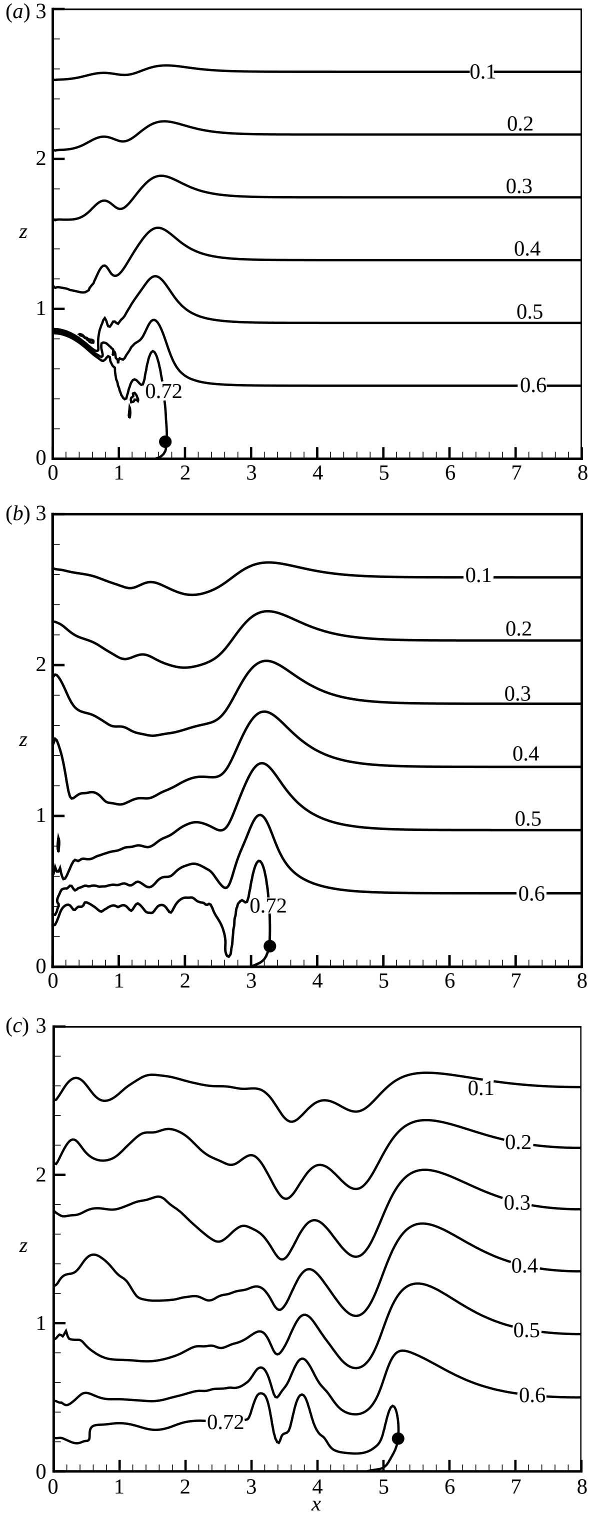

FIGURE 8. Numerical results: contour lines of the density function ϕ at (*a*) $t = 2$, (*b*) 6 and (*c*) 12 for Run 19. The dot marks the 'nose'. (Recall that, initially, in the dense fluid $\phi = 1$, while in the ambient $\phi = 0$ at the top and $\phi = 0.72$ at the bottom).

configuration. This theory predicts well the propagation of currents of the first class, and also the propagation of currents of the second class until the determined position x_2. We showed that the NS simulations are in good agreement with experimental observations concerning the wave–head interaction of the subcritical current. These results have advanced the knowledge on two-dimensional gravity currents in a stratified ambient and will serve as a good starting point for further work, both theoretical and experimental.

3. Axisymmetric and rotating cases

In this section, we consider the current to be released from a cylindrical lock of height h_0 and radius r_0, and the entire system to be rotating with a constant angular velocity Ω about the vertical axis z (with $\Omega = 0$ as a particular case). We use a cylindrical coordinate system, $\{r, \theta, z\}$, co-rotating with the ambient fluid. The velocity components in the rotating system are $\{u, v, w\}$ and we assume that the flow does not depend on the angular coordinate θ. In the meridional plane r, z the current is similar to that sketched in figure 1, but, in addition: (i) the geometry diverges with r; (ii) there is motion in the azimuthal direction; and (iii) the rotation of the system about z introduces centrifugal-Coriolis forces.

It is convenient in this section to scale the dimensional variables (denoted here by asterisks) by

$$\{r^*, z^*, h^*, H^*, t^*, u^* v^*\} = \{r_0 r, h_0 z, h_0 h, h_0 H, Tt, Uu, \Omega r_0 v\}, \tag{3.1}$$

where

$$U = (h_0 g')^{1/2}, \quad T = r_0/U. \tag{3.2}$$

We also define the angular velocity (in the rotating system)

$$\omega = v/r, \tag{3.3}$$

a dimensionless variable scaled with Ω.

As compared to the previously considered two-dimensional case, two extensions of the SW equations of motion are necessary. First, the geometrical curvature terms must be incorporated, which is a quite straightforward task. Secondly, for $\Omega > 0$, the azimuthal momentum equation and Coriolis-centrifugal terms must be added to the formulation. The relevant dimensionless parameter is the typical Coriolis to inertia ratio

$$\mathscr{C} = \frac{\Omega r_0}{(g' h_0)^{1/2}}. \tag{3.4}$$

This parameter does not take into account the stratification of the ambient. We shall prove later that the effect of Coriolis forces is more pronounced when S increases (and, actually, the inertia of propagation in the radial direction decreases.) We are interested in small values of $\mathscr{C}$; otherwise, the Coriolis effects restrict the propagation to a small distance and no real gravity current develops. On the other hand, when $\mathscr{C}$ is small the deviation of the current from the initial solid-body-rotation is significant, i.e. the Rossby number of the flow is not small. We note in passing that an important parameter in stratified rotating fluids is the ratio of the usual buoyancy frequency of the ambient, $\mathscr{N}$, to $f = 2\Omega$. This is related to our parameters by

$$\frac{f}{\mathscr{N}} = \frac{2}{\sqrt{S}} \frac{h_0}{r_0} \mathscr{C} \sqrt{H}. \tag{3.5}$$

The one-layer model is used, again, for simplicity. A hydrostatic–cyclostrophic pressure balance is assumed in the motionless ambient, and a vertical hydrostatic balance in the dense fluid. After some algebra, it turns out that in the range of parameters considered here (in particular $\epsilon \ll 1$ and $\mathscr{C} < 1$) the relationship between the lateral pressure gradient and inclination of the interface is similar to the two-dimensional case, and the z-averaged azimuthal momentum balance and Coriolis interaction are similar to the non-stratified case, as discussed by Ungarish & Huppert (1998). The internal waves are, again, not incorporated in the SW formulation for the reasons mentioned above.

In conservation form, the averaged balance equations of continuity, radial momentum and azimuthal momentum can be written as

$$\frac{\partial h}{\partial t} + \frac{\partial}{\partial r}(uh) = -\frac{uh}{r}, \tag{3.6}$$

$$\frac{\partial}{\partial t}(uh) + \frac{\partial}{\partial r}\left[u^2 h + \tfrac{1}{2}(1-S)h^2 + \tfrac{1}{3}S\frac{h^3}{H}\right] = -\frac{u^2 h}{r} + \mathscr{C}^2 vh\left(2 + \frac{v}{r}\right), \tag{3.7}$$

and

$$\frac{\partial}{\partial t}(vh) + \frac{\partial}{\partial r}(uvh) = -2uh\left(1 + \frac{v}{r}\right) \tag{3.8}$$

which in characteristic form become

$$\begin{bmatrix} h_t \\ u_t \\ v_t \end{bmatrix} + \begin{bmatrix} u & h & 0 \\ 1 - S + S\dfrac{h}{H} & u & 0 \\ 0 & 0 & u \end{bmatrix} \begin{bmatrix} h_r \\ u_r \\ v_r \end{bmatrix} = \begin{bmatrix} -uh/r \\ \mathscr{C}^2 v(2 + v/r) \\ -u(2 + v/r) \end{bmatrix}. \tag{3.9}$$

The first two characteristic velocities of this system $\mathrm{d}r/\mathrm{d}t = c_\pm$ are given by (2.16) as in the two-dimensional case, but the balance on the characteristics is modified by the curvature and Coriolis terms so that

$$\mathrm{d}h \pm \frac{1}{a(h)}\,\mathrm{d}u = \mathrm{d}t\left[-\frac{uh}{r} \pm \frac{1}{a(h)}\mathscr{C}^2 v\left(2 + \frac{v}{r}\right)\right]. \tag{3.10}$$

The third characteristic velocity is $\mathrm{d}r/\mathrm{d}t = u$ and the corresponding balance can be used to derive the boundary condition for ω at the nose, (3.14).

The initial conditions are zero velocity in both radial and azimuthal directions, and unit dimensionless height and length at $t = 0$. Also, for $t > 0$, the velocity at $r = 0$ is zero, and the boundary conditions for the variable h can be evaluated from the characteristics which propagate from the interior with c_- and c_+ to $r = 0$ and r_N, respectively.

Boundary conditions for the radial and azimuthal (angular) velocity components at the nose $r = r_N(t)$ are required. We argue that for small values of $\mathscr{C}^2$, the boundary conditions for u_N are as in the two-dimensional case, and we shall therefore use (2.17) and (2.18). This assumption is vindicated by the good agreement of the $r_N(t)$ predicted by the present SW formulation with full NS computation and laboratory experiments, as discussed in § 3.2. (The formulation of the boundary condition for the propagation of the nose of the gravity current when $\mathscr{C}^2$ is not small is beyond our scope, because in this case the distance of propagation is typically less than 1 and hence the resulting flow is not truly a gravity current, but rather an adjusting bulk of rotating fluid.)

Concerning the angular velocity, we note that the foregoing equations of motion yield conservation of potential vorticity, which reads

$$\frac{\mathrm{D}}{\mathrm{D}t}\left(\frac{\zeta+2}{h}\right)=0, \tag{3.11}$$

where

$$\zeta=\frac{1}{r}\frac{\partial}{\partial r}(r^2\omega) \tag{3.12}$$

is the axial vorticity component (scaled with Ω), see for example Ungarish & Huppert (1998). On account of the initial conditions, the conservation of potential vorticity can be reformulated as

$$h=1+\tfrac{1}{2}\zeta. \tag{3.13}$$

A combination of the total volume conservation of the dense fluid, (3.13) and (3.12) yield the boundary condition

$$\omega=-1+\left(\frac{1}{r_N(t)}\right)^2 \quad (r=r_N). \tag{3.14}$$

The same result can be obtained by following the balance on the aforementioned third characteristic starting at $r=1$, as presented in Ungarish & Huppert (1998).

3.1. *Steady lenses* (*SL*)

For $\mathscr{C}>0$, the system (3.9) admits a non-trivial steady-state solution with $u=0$ and $r_N=\text{constant}$. This reflects an equilibrium between the pressure and Coriolis-centrifugal forces (actually, a strongly-idealized situation, because both viscous effects and residual motion from the initial propagation are neglected). The task is to determine $h(r)$, $\omega(r)$ and r_N of the possible steady lens (SL). These flows have important applications in oceanography (Csanady 1979; Hedstrom & Armi 1988).

Letting $y=r/r_N$, we can express the radial momentum and potential vorticity equations, (3.7) and (3.13), for $0\leqslant y\leqslant 1$, as

$$A\frac{\mathrm{d}h}{\mathrm{d}y}=\mathscr{C}^2r_N^2y[\omega(2+\omega)], \tag{3.15}$$

$$h=1+\omega+\tfrac{1}{2}y\frac{\mathrm{d}\omega}{\mathrm{d}y}, \tag{3.16}$$

where

$$A=1-S+S\frac{h}{H}, \tag{3.17}$$

subject to the boundary conditions (3.14), regularity at $y=0$ and $h(y=1)=0$. Substitution of (3.16) into (3.15) yields a single equation for ω. The solution provides r_N of the lens, $\omega(y)$ and $h(y)$. For the non-stratified case, $S=0$, which is obviously the simplest one because $A=1$, numerical and approximate analytical solutions have been presented (see Ungarish & Zemach 2003 where other references are given). The stratified system is complicated by the additional parameter S; in particular, for $S=1$ we obtain $A=h/H$, and a singularity of (3.15) at $y=1$ appears owing to the conditions $h(1)=0$. The influence of S is clarified by the following results.

3.1.1. *Analytical approximations*

The first type of approximate solution can be derived when $\mathscr{C}\ll 1$ and $1-S\gg\mathscr{C}$ (i.e. S is not very close to 1). An expansion in powers of $\mathscr{C}$ indicates that $h\sim\mathscr{C}$, and hence, to leading order, $A = 1 - S$ is a positive constant. This reduces, to leading order in $\mathscr{C}$, the present problem (3.15)–(3.16) to that of a non-stratified case, but with a modified Coriolis coefficient

$$\mathscr{C}_m = \mathscr{C}(1 - S)^{-1/2}. \tag{3.18}$$

Following Ungarish & Huppert (1998) (see also Ungarish & Zemach 2003), we readily obtain the approximation

$$h = \mathscr{C}_m(1 - y^2), \tag{3.19}$$

$$\omega = -1 + \mathscr{C}_m\left(1 - \tfrac{1}{2}y^2\right), \tag{3.20}$$

and

$$r_N = (2/\mathscr{C}_m)^{1/2}. \tag{3.21}$$

We are interested in cases with small $\mathscr{C}_m$ because otherwise the distance of propagation is small, see (3.21), and no real gravity current appears. As could be expected, the stratification decreases the pressure gradients and hence increases the relative importance of the Coriolis effects. The lens is thin, $O(\mathscr{C}_m)$, and practically 'feels' the ambient fluid in the proximity of the bottom whose density is ρ_b. The resulting lens is like one produced in a homogeneous case with density difference $\rho_c - \rho_b$. The approximation (3.18)–(3.21) evidently diverges when S approaches 1, i.e. $\rho_c - \rho_b$ vanishes, and hence a different expansion is required for this case, as follows.

The second type of approximate solution can be derived when $S = 1$ and $\mathscr{C}^2 H \ll 1$. The density difference between the lens and the ambient is small, and hence, as compared with the previous case, a thicker lens, a smaller radius and a stronger slope of the interface are required to counterbalance the Coriolis effects. An order of magnitude consideration indicates that here $h(y)$ and $\omega(y) + 1$ can be expanded in powers of $(\mathscr{C}^2 H)^{1/3}$. Substitution of this expansion in the governing equation, subject to volume conservation and boundary conditions yields, to leading order,

$$h = (\mathscr{C}^2 H)^{1/3}\left(\tfrac{3}{2}\right)^{1/3}(1 - y^2)^{1/2}, \tag{3.22}$$

$$\omega = -1 + (\mathscr{C}^2 H)^{1/3}\left(\tfrac{2}{3}\right)^{2/3}\left[1 - (1 - y^2)^{3/2}\right]\frac{1}{y^2}, \tag{3.23}$$

and

$$r_N = \left(\tfrac{3}{2}\right)^{1/3}(\mathscr{C}^2 H)^{-1/6}. \tag{3.24}$$

As $y \to 1$, $h'(y)$ and $\omega''(y) \to \infty$, but $|\omega'(y)|$ is small; a local and relatively small contribution of viscous or turbulent dissipation effects is expected to develop. We are interested in cases with small $\mathscr{C}^2 H$ because otherwise the distance of propagation is small, see (3.24), and no real gravity current appears.

When $S = 1$, the dimensionless parameter $\mathscr{C}^2 H$ can also be expressed as $(\Omega r_0 \mathscr{N} h_0)^2 = (f r_0 / 2\mathscr{N} h_0)^2$, where, again, $\mathscr{N}$ is the usual buoyancy frequency of the ambient, and $f = 2\Omega$, see (3.5). The foregoing approximations yield the following compact results for the radius of propagation and aspect ratio of the lens in the $S = 1$ case

$$\frac{r_N^*}{V^{*\,1/3}} = \left(\frac{3}{\pi}\frac{\mathscr{N}}{f}\right)^{1/3}, \tag{3.25}$$

$$\frac{h^*(0)}{r_N^*} = \frac{1}{2}\frac{f}{\mathscr{N}}, \tag{3.26}$$

where V^* is the volume of the lens (the upper asterisks denotes dimensional variables). It is remarkable that the shape of the lens is determined only by the volume and $f/\mathcal{N}$; the details of the initial aspect ratio h_0/r_0 do not influence the results (to leading order).

The case $S=1$ is related to the lenses produced by intrusion in a stratified fluid at a neutral level, i.e. at the horizontal midplane $z=0$, the densities of the ambient and intruding fluid are equal, which corresponds to $\epsilon_b=\epsilon$, or $S=1$, in our study. The aspect ratio of the height to radius of the lens provided by the present approximation (3.26) is in full agreement with the result that has been theoretically predicted and experimentally confirmed for the neutral level intrusion lens from a point source of non-rotating fluid (Gill 1981; Griffiths & Linden 1981; Hedstrom & Armi 1988). Actually, for a small value of $\mathscr{C}^2 H$ (as assumed here) the present constant-volume lens spreads significantly. Therefore its angular velocity is reduced to almost -1, see (3.23), and hence the features of a lens of non-rotating fluid are a good approximation.

The foregoing results are also useful in the energy balance considerations. The pertinent potential (in the reduced-gravity field) and kinetic energies, scaled with $\rho_o g' r_0^2 h_0^2$ (per radian) can be expressed as:

$$PE = r_N^2 \int_0^1 \left[\tfrac{1}{2}(1-S)h^2(y) + \frac{1}{6}\frac{S}{H}h^3(y) \right] y\,\mathrm{d}y, \tag{3.27}$$

$$EK = \tfrac{1}{2}\mathscr{C}^2 r_N^4 \int_0^1 (1+\omega(y))^2 h(y) y^3\,\mathrm{d}y. \tag{3.28}$$

(The kinetic energy in the initial and SL stages is contributed by the azimuthal velocity only because there is no radial motion in these situations.) In the initial state, $h=1$, $r_N=1$ and $\omega=0$, and hence

$$E = PE + KE = \tfrac{1}{4}(1-S) + \frac{1}{12}\frac{S}{H} + \tfrac{1}{8}\mathscr{C}^2 \quad (t=0). \tag{3.29}$$

As expected, the stratification reduces the potential energy in the initial system. The energy in the SL is obtained by substituting the appropriate $h(y)$ and $\omega(y)$ in (3.27)–(3.28). Using the approximations (3.19)–(3.24), we find: (i) for $S<1$

$$E = \mathscr{C}_m \left[\tfrac{1}{6}(1-S) + \mathscr{C}_m \frac{1}{24}\frac{S}{H} \right] + \tfrac{23}{240}\mathscr{C}_m^3(1-S); \tag{3.30}$$

and (ii) for $S=1$

$$E = \tfrac{1}{20}\left(\tfrac{3}{2}\right)^{2/3} \frac{1}{H}(\mathscr{C}^2 H)^{2/3} + 0.120\frac{1}{H}(\mathscr{C}^2 H)^{4/3}. \tag{3.31}$$

The last term in (3.29)–(3.31)) represents the kinetic energy. We conclude that for the cases considered here (small $\mathscr{C}_m$ for $S<1$ and small $\mathscr{C}^2 H$ for $S=1$) the energy of the SL is significantly smaller than in the initial state. The potential energy is the dominant term in both the SL and initial states. The difference with the lens created by slow injection mentioned above is the need to dissipate the energy excess.

For given $\mathscr{C}$, the radius r_N decreases with S according to (3.21), and at some value of S the radius r_N predicted by (3.24) is reached. This point of intersection provides the estimate of the limit of validity of (3.21). This yields

$$S < 1 - 0.43(\mathscr{C}/H)^{2/3}, \quad \mathscr{C}_m < 1.5(\mathscr{C}^2 H)^{1/3}, \tag{3.32}$$

which is actually a very mild restriction on the applicability of the approximations (3.20)–(3.21). We conclude that the approximations developed here are expected to cover practically the entire range of S of interest. This has been confirmed by comparison with the more accurate results considered next.

3.1.2. *Numerical solutions*

In general, the determination of the SL system must be performed by numerical methods, which include iterations on the nonlinear right-hand side of (3.15) and value of r_N. We used a finite-difference discretization on a 100 interval grid, and performed iterations (from some initial guess guided by the foregoing approximate results) for obtaining the proper nonlinear combination of $\omega(y)$, $h(y)$ and r_N which satisfies the equations and converges to the boundary condition $h(1)=0$.

The $S=1$ case requires special attention. The straightforward finite-difference approach fails in the corner region where y approaches 1, because of the singularity which shows up as $A=h/H$ tends to 0 and the slope of h becomes very large. However, ω remains regular, and hence for y close to 1 (3.15), subject to (3.14), can be approximated by

$$\frac{1}{2H}\frac{\mathrm{d}h^2}{\mathrm{d}y} = -\mathscr{C}^2 r_N^2\left(1-\frac{1}{r_N^4}\right) = -\beta, \tag{3.33}$$

which yields

$$h = [2H\beta(1-y)]^{1/2}, \tag{3.34}$$

and this expression is used in the last grid interval of the numerical solution instead of the difference equation for h.

Typical results of the SL shape and internal angular velocity are presented in figure 9. As the stratification (value of S) increases, the lens becomes thicker and shorter and the retrograde angular velocity in the interior decreases. The $S=1$ case, despite the singularity, does not display any qualitative dissimilarity with the other cases. The agreement between the analytical approximate results and the numerical solution of the SL is good. The approximations were developed for small values of $\mathscr{C}$ and $\mathscr{C}^2H$; in figure 9(*b*) these parameter are not so small, $\mathscr{C}=0.4$ and $\mathscr{C}^2H=0.48$, yet fair agreement is obtained for h in all cases (this also implies agreement for r_N) and for ω for $S \leqslant 0.5$ (in figure 9*a*, $\mathscr{C}=0.3$ and $\mathscr{C}^2H=0.18$ and the agreement is very good for all the predicted variables in the full range of S). We conclude that the analytical result captures well the parametric behaviour of the flow field. The stability of the lens and its dissipation by viscous and mixing effects (expected to be governed by localized three-dimensional instabilities) are important features that deserve future investigation.

3.2. *Results and comparisons for axisymmetric and rotating cases*

The effect of stratification on the propagation of a typical rotating axisymmetric gravity current, as predicted by the SW formulation, is shown in figure 10. The predictions for the interface are shown in figure 11. As expected, the Coriolis effects hinder, and eventually stop, the radial propagation. The Coriolis-influenced interface develops a downward inclination of the frontal region, and the height of the nose decays to zero in a relatively short time. As expected, when S increases, both the speed of radial propagation and the maximum radius of spread are significantly reduced. The interpretation of this trend is as follows.

The increase of S decreases the effective reduced gravity that drives the nose, g'_e, defined (approximately) by UH as

$$g'_e = \frac{\rho_c - \rho_a(z=0.5h_N)}{\rho_o}g = g'\left[1 - S\left(1-\frac{h_N}{2H}\right)\right]. \tag{3.35}$$

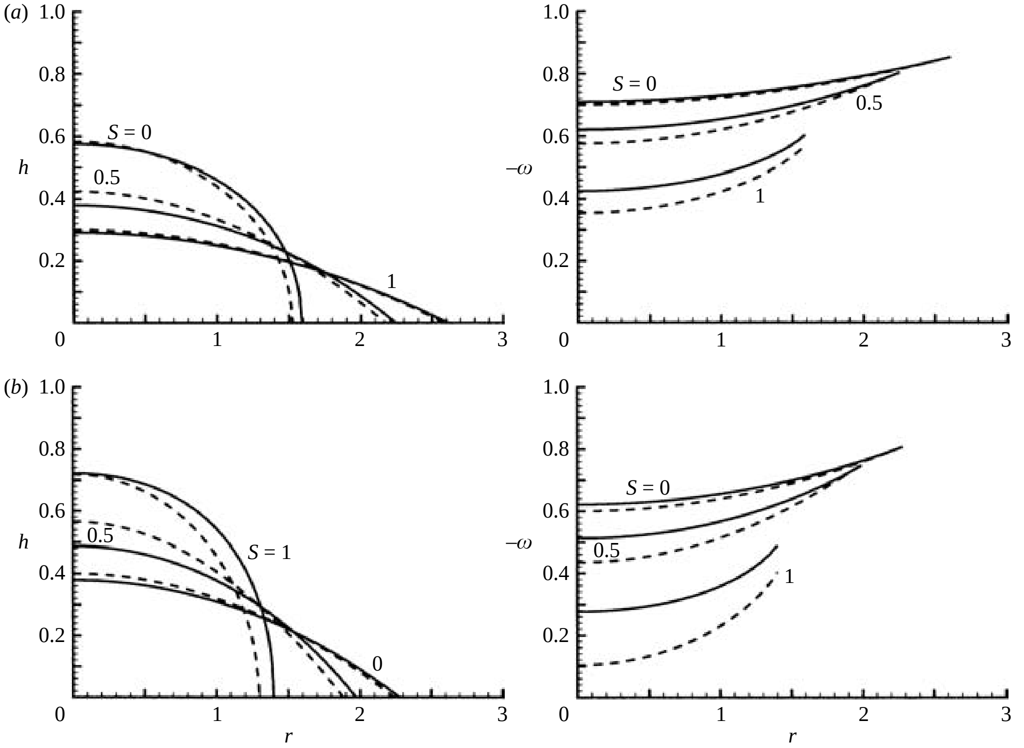

FIGURE 9. Lens behaviour h and ω as functions of r and various S, for (a) $\mathscr{C} = 0.3$, $H = 2$ and (b) $\mathscr{C} = 0.4$, $H = 3$. Numerical solution (solid lines) and approximate solution (dashed lines).

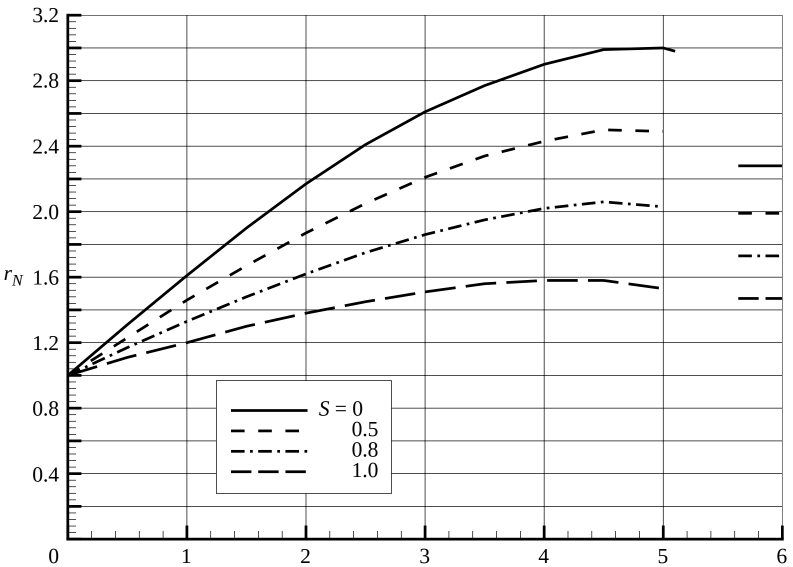

FIGURE 10. SW results for the propagation of gravity currents rotating with $\mathscr{C} = 0.4$ and $H = 3$ for various ambient stratifications. The horizontal lines on the right of the graph show the SL asymptote.

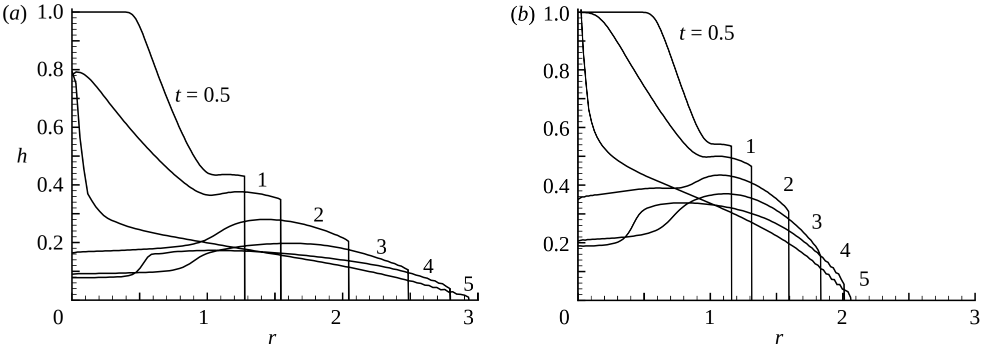

FIGURE 11. SW predicted profiles of h as a function of r at various times for the rotating gravity currents with $\mathscr{C} = 0.4$ and $H = 2$, for (*a*) $S = 0$ and (*b*) $S = 0.8$.

The approximation is based on the observation that the nose reacts to the density difference at about half-height. Thus, the initial radial propagation is expected to decrease with S, as in the case of a two-dimensional current, simply because the driving density difference decreases with S. On the other hand, the Coriolis-centrifugal forces are not influenced by the axial stratification. This suggests the introduction of an effective Coriolis dimensionless parameter, see (3.4)

$$\mathscr{C}_e = \frac{\Omega r_0}{(g_e' h_0)^{1/2}} = \mathscr{C}\left[1 - S\left(1 - \frac{h_N}{2H}\right)\right]^{-1/2}. \tag{3.36}$$

During the initial propagation, the typical value of h_N is 0.5, then it decreases, and hence the effective $\mathscr{C}_e$ is larger than the formal $\mathscr{C}$ for $S > 0$ all the time. Moreover, eventually the Coriolis effects reduce h_N to zero and the propagation stops. This further enhances the effect of stratification because the nose is brought down to encounter levels of larger and larger density. We expect that at this stage of slow radial propagation the dynamic behaviour switches to the equilibrium mode, i.e. the SL balances become relevant, in particular the maximum r_N predicted by (3.21) and (3.24); indeed, for $h_N = 0$ we obtain $\mathscr{C}_e = \mathscr{C}_m$, see (3.18). Note that $\mathscr{C}_e$ is associated with the dynamic propagation, and $\mathscr{C}_m$ with the equilibrium lens.

An inspection of the SW results presented in figure 10 confirms this interpretation. Moreover, figure 10 indicates that no special behaviour appears when $S = 1$, although the SL radial momentum balance (3.15) has a singularity at r_N in this case. We infer that this is a local singularity which does not alter the behaviour in the interior. The analysis of these and similar SW results for different values of $\mathscr{C}$ and H lead to the following conclusions: the maximum radius of propagation attained by the current exceeds the radius of the SL; the excess varies from about 30% for $S = 0$ to about 20% for $S = 1$. The time at which the maximum propagation is attained is given (approximately) by $1.7/\mathscr{C}$ for $S = 0$ and decreases (slightly) as S approaches 1. The interval $\mathscr{C}t \approx \pi/2$ from release to the maximal propagation corresponds to about a quarter-revolution of the system. The fact that the stratification has little influence on this time interval is an interesting outcome, that can be explained by the fact that as S increases, both the maximum radius and the velocity of propagation decrease, so that the (mean) ratio of distance over velocity remains unchanged. The prediction that the maximum SW radius is larger than that of the SL indicates that some contraction and oscillations are expected after $t = 1.7/\mathscr{C}$, for any S. In the stratified case the classical oscillations of the bulk of dense fluid about the steady-lens form are

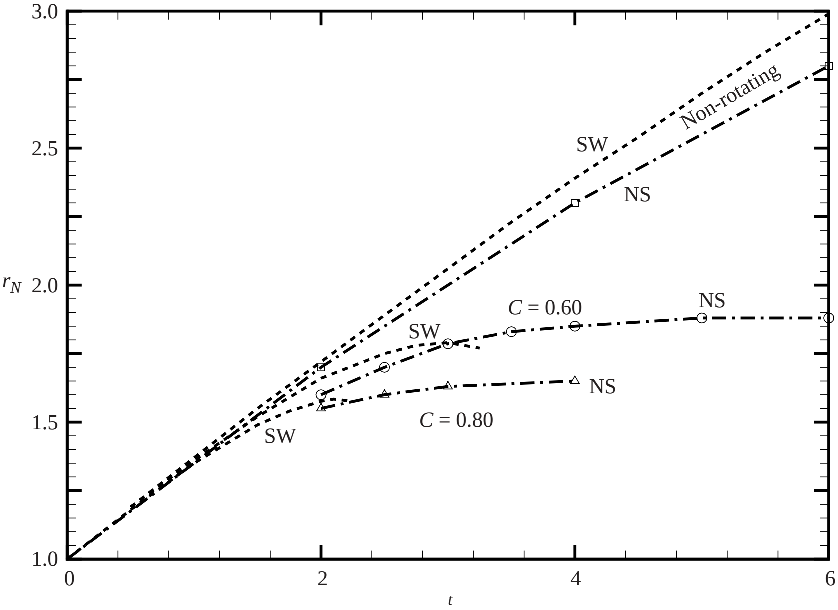

FIGURE 12. The propagation of axisymmetric gravity currents in a stratified ambient $S = 0.72$ and $H = 3$. NS (symbols and dash-dotted lines) and SW (dashed lines) predictions for $\mathscr{C} = 0.8, 0.6$, and 0 (non-rotating).

expected to combine with oscillations of the isopycnals in the ambient. The Ekman layers develop in about one revolution of the system, and hence are not expected to have an influence during the propagation to maximum radius that is attained in a shorter time interval. Eventually, these layers and other dissipative mechanisms will smooth out the discontinuity of ω between the lens and the ambient.

We conclude that our interpretations capture well the combined effects of rotation and stratification. (Recall that the analysis is for small values of $\mathscr{C}$ in general, and for small $\mathscr{C}\sqrt{H}$ when S is close to 1.) The interaction between the nose and the internal waves is expected to develop as in the two-dimensional case, but complicated by the effects of curvature and Coriolis (inertial waves). Typically, the velocity of axisymmetric currents decays faster than that of two-dimensional currents, and the rotation enhances this trend. We therefore speculate that the major stage of inertia-dominated propagation will be close to its end before the internal waves become influential. This is consistent with the numerical and experimental results presented below, but this topic requires a great deal of additional investigation that must be left for future work.

To corroborate the SW prediction, we perform now some comparisons with the NS numerical solutions. The configuration is the axisymmetric counterpart of the two-dimensional computation for Run 19 considered above, i.e. the same values of $\epsilon = 0.0804$, $S = 0.72$, $H = 3$ and lock aspect ratio $h_0/r_0 = 0.25$. The outer wall of the computational domain was at $r_w = 8$, a grid of 320×200 intervals was used and $Re = 3.85 \times 10^4$. Runs for non-rotating, and for rotation with $\mathscr{C} = 0.6$ and 0.8 were performed.

The predictions of r_N as functions of t are shown in figure 12. The propagation calculated via the SW model is slightly faster than that obtained from the NS computation (owing to viscous and mixing effects), but the agreement is still very good. The difference between the non-rotating and rotating systems is evident: the Coriolis effects drastically limit the propagation. It is clear that as $\mathscr{C}$ increases the maximum radius of propagation decreases and is attained in a shorter time.

To be specific, the SW predicted maximum r_N of 1.80 and 1.60 for $\mathscr{C}=0.6$ and 0.8, respectively, is attained at $t=3.0$ and 2.1 (in both cases at $t\mathscr{C}\approx 1.6$). The corresponding NS results attain quasi-maximum radii of 1.8 and 1.6 at $t=3.0$ and 2.5. By quasi-maximum we mean that the typical head of the current vanishes (this is inferred from the shape and behaviour of the interface between the dense fluid and the ambient); the rim of the current still advances very slowly, but its motion seems to be dominated by viscous and diffusion effects. The fact that the NS (and experimental) currents lack a sharp maximum radius of propagation, and actually display a slow spread of the rim after the end of the inertia-Coriolis propagation has been observed and reported also for non-stratified circumstances (Verzicco, Lalli & Campana 1997; Hallworth *et al.* 2001). Viscous effects could be expected to be important when the radial motion of the edge becomes slow and the height there is small, and this explains the reason for and the trend of the discrepancy with the inviscid SW results for $t > 1.6/\mathscr{C}$, approximately. Otherwise, the agreement with the SW model is very good concerning the radius and time of propagation of the major motion and the influence of the dimensionless parameters.

The present configuration is subcritical from the beginning of the motion, see figure 2. Yet we observe that the stratification waves have no significant effect on the motion in the time intervals (or distances of propagation) considered here. Indeed, in the two-dimensional case, see figure 7, the interaction developed at $t=12$, after a propagation of about five lock lengths, whereas in the present rotating axisymmetric cases the maximum radius is reached at $t\approx 3$ and the propagation is about one lock length. In the axisymmetric non-rotating case some hindering of the nose shows up in the NS computation at $t=12$, but this is not a clear-cut wave effect like in the two-dimensional counterpart. The mean thickness of the axisymmetric current decreases like $1/r_N$, and at $t=10$ is about one tenth of its initial value, while the area of contact with the bottom is about ten times larger then that of the lock. This evidently enhances the relative contribution of viscous friction, and it is difficult to distinguish between this effect and wave hindering of the nose at these times. In any case, the wave–head interaction in the axisymmetric current does not develop sooner than in the two-dimensional counterpart.

The dramatic effect of rotation and the complex shape of the interface are illustrated in figure 13. Contour lines of the density function of value $\phi = 0.72$, obtained from the NS simulations, are plotted at various times for the non-rotating case and for the rotating with $\mathscr{C} = 0.6$ case. At $t = 2$, the difference between the cases is small, but afterwards the Coriolis effects dominate the second case. The non-rotating current spreads out for a long time, while the height of the head is reduced gradually (the effective Reynolds number decays like (u_N/r_N) and at $t=14$ the viscous effects are already important and hinder the propagation). In contrast, the bulk of the rotating current spreads out very little and during a relatively short time only; the bulk of dense fluid even thickens at $t=4$ (this indicates a reverse motion in the centre). Similar features have been reported for a non-stratified ambient; the stratification enhances the differences between the non-rotating and rotating cases in the sense that the maximum radius of propagation decreases with S.

Corresponding SW predictions are shown in figure 14. There is fair agreement in the global behaviour, in particular concerning the effect of the rotation on the behaviour of the current. The negative radial velocity in the rotating current at $t = 3$

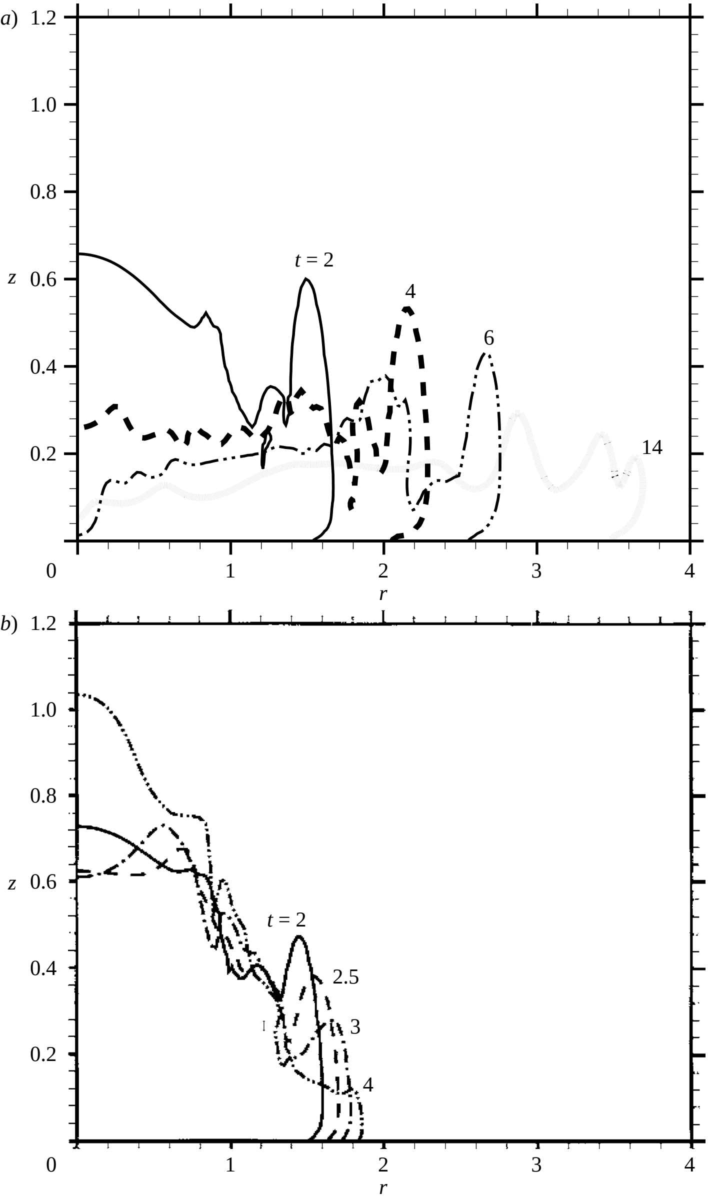

FIGURE 13. NS predictions: the interface of axisymmetric gravity currents for various times, in (*a*) non-rotating and (*b*) rotating with $\mathscr{C} = 0.6$. In both cases $S = 0.72$ and $H = 3$.

has no counterpart in the non-rotating situation. The NS simulations produce, as expected, more complex profiles than the SW approximations, but the same type of discrepancy was noted for the non-stratified ambient too, see Hallworth *et al.* (2001).

The predicted behaviour of the angular velocity in the rotating current is displayed in figure 15. The NS simulations show that the current has a distinct signature of negative ω during its propagation. There is, again, fair agreement with the SW approximations. The discrepancies can be attributed to the differences in the local height of the interface, deviations from the one-dimensional motion and the friction

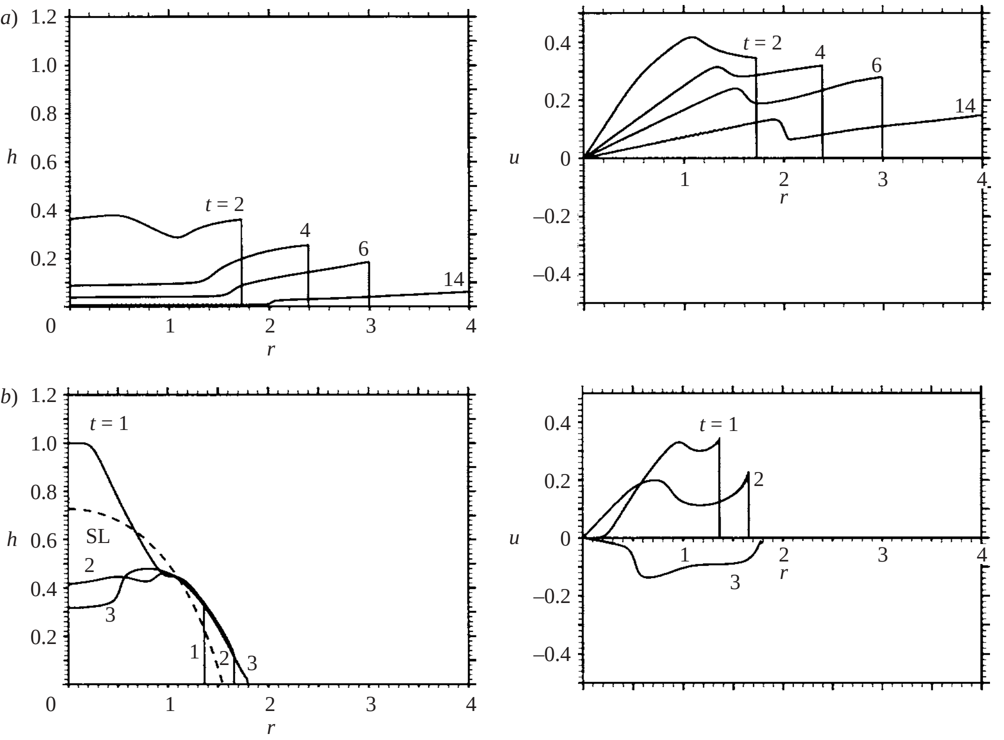

FIGURE 14. SW predictions: the interface and radial velocity of axisymmetric gravity currents for various times, in (*a*) non-rotating and (*b*) rotating with $\mathscr{C} = 0.6$. In both cases $S = 0.72$ and $H = 3$. The steady lens interface profile is shown by the dashed line.

on the boundary and interface. Again, similar discrepancies have been detected in the non-stratified cases. The SW results predict that the expansion is completed at $t \approx 1.6/\mathscr{C} = 2.7$. Indeed, at $t = 2$ and 3 we observe the typical negative angular momentum, but at $t = 4$ we find a significant increase of ω in the dense fluid. This change can be attributed to the reverse (contraction) radial motion of the current. This reverse motion in the dense fluid is also clearly confirmed by the ascent of the interface near the centre at $t = 4$, see figure 13.

The motion of the interface at the centre provides a convenient detector of the expansion–contraction oscillations that appear in the bulk of the dense fluid. This is illustrated in figure 16. In addition to the $S = 0.72$ case discussed above, we also show the lesser stratified $S = 0.43$ and the non-stratified $S = 0$ counterparts (in all cases $H = 3$ and $\mathscr{C} = 0.6$). In all cases, the height of the interface at the centre first decreases and reaches a minimum at $t \approx 2.7$; this corresponds to the maximum expansion which is expected to occur, according to the SW estimate, at $t \approx 1.6/\mathscr{C} = 2.7$. Afterwards, up and down oscillations appear, and the period of this motion depends on the value of S. In the non-stratified case, the inertial period $T_p = \pi/\mathscr{C} = 5.2$ (in dimensional units, π/Ω) is expected to be relevant. The experiments of Hallworth *et al.* (2001) (for a non-stratified ambient) detected oscillation with the period of $T_p\mathscr{C} = 3.0$. On the other hand, the period of the internal gravity waves is $2\pi(h_0/r_0)(H/S)^{1/2}$, i.e. 3.2 for $S = 0.72$ and 4.1 for $S = 0.43$. We thus see that the oscillations in the stratified cases display shorter periods, in qualitative agreement with the foregoing estimates. Because of possible interactions between the waves and viscous damping, a detailed

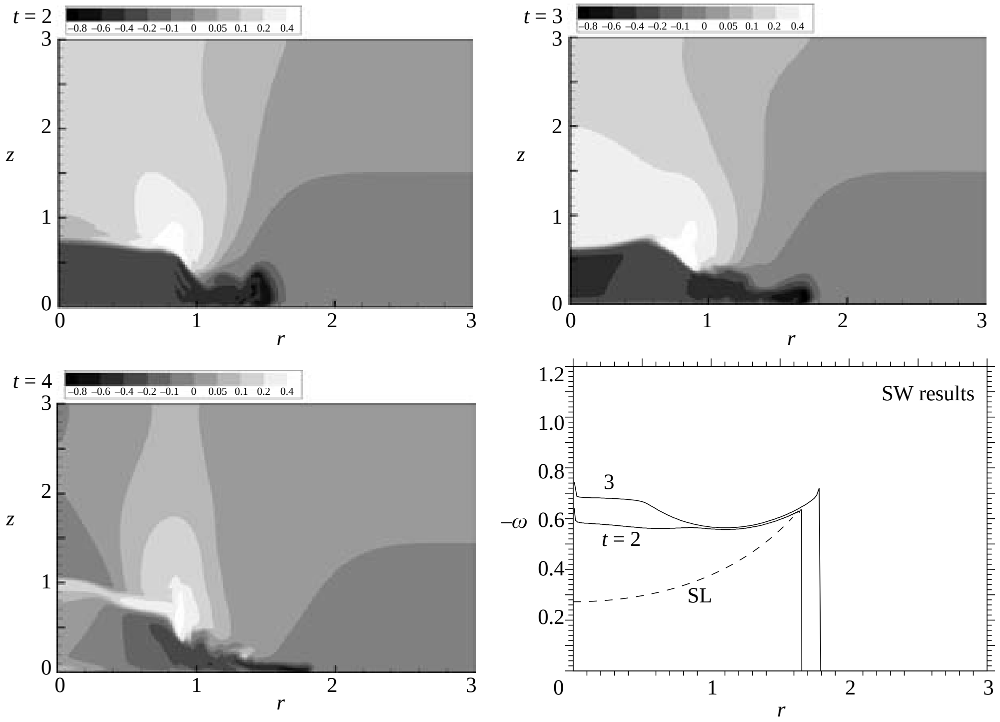

FIGURE 15. The angular velocity for $\mathscr{C} = 0.6$, $H = 3$, $S = 0.72$ configuration. NS prediction contours, and SW prediction (including SL) profiles for various times.

quantitative comparison is outside the scope of this work. However, we note that the time interval between the first minimum and the first peak is (approximately) 1.6, 2.1 and 2.4 for $S = 0.72, 0.43$ and 0, respectively; the first two correspond to the half-period of the internal waves, the last one to the half-period of the inertial modes. Moreover, the initial amplitude of the internal waves is larger, because the isopycnal of the interface tends to return to the initial position of equilibrium $h = 1$ (and the initial displacement is about 0.55 in the present cases), while the inertial oscillations tend to be driven by the displacement from the SL equilibrium (which is about 0.15 in the present cases).

To summarize, the SW approximation for the axisymmetric rotating current in a stratified ambient is consistent with the NS simulations for the initial period of propagation (until Coriolis or viscous forces become dominant). The discrepancies between the SW and NS results are similar to these obtained for the situation of a homogeneous ambient in corresponding cases. In other words, the incorporation of the stratification in the present SW model does not reduce the intrinsic accuracy of this type of analysis for the cases under consideration.

Experimental verifications of these predictions are also important, in particular that concerning the stability of the rotating current. It is known that strong three-dimensional instabilities develop for surface gravity currents in a rotating system, and eventually the central core breaks into smaller, non-axisymmetric structures, see Griffiths & Linden (1981). These effects have been reproduced numerically for a non-stratified ambient by Verzicco *et al.* (1997). However, there are indications that for bottom currents and small $\mathscr{C}$, as considered here, the growth of the instabilities is slow,

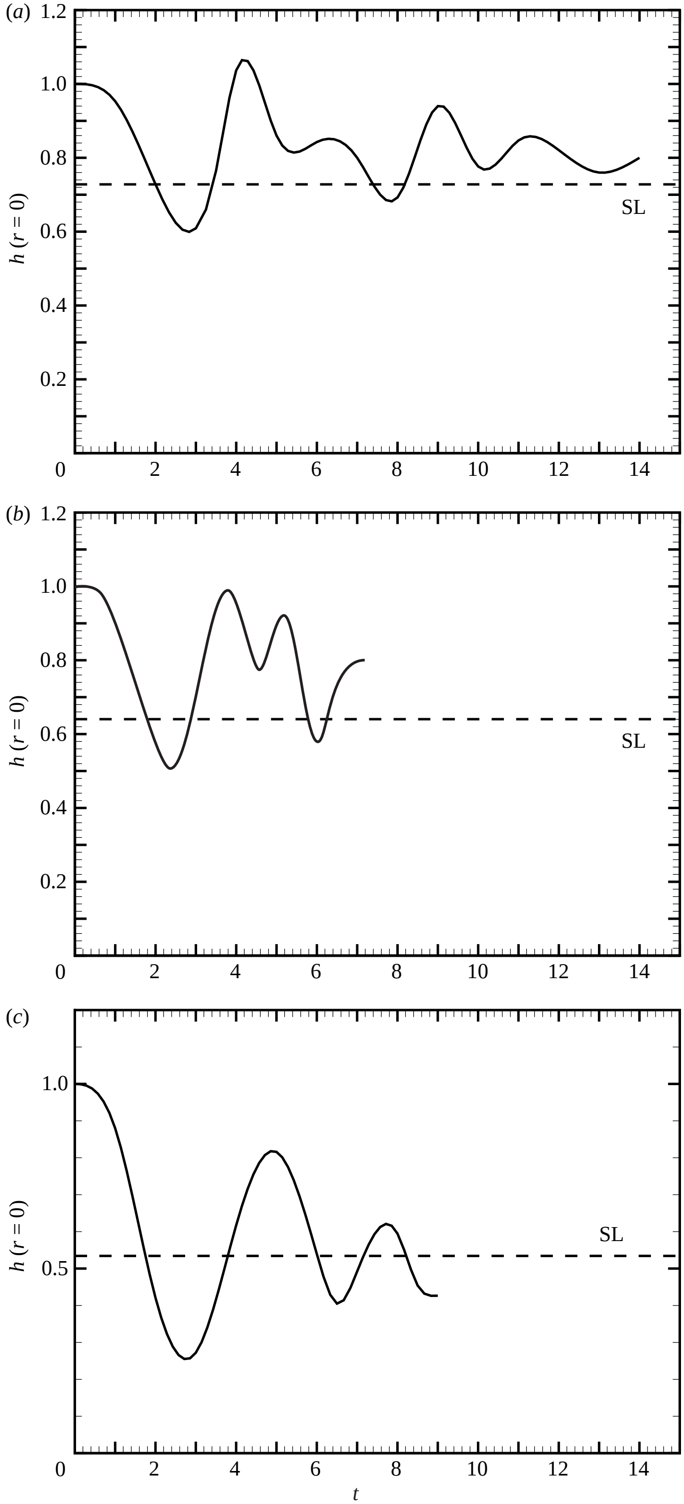

FIGURE 16. The oscillations as reflected by height of the interface at the centre as a function of t for $\mathscr{C} = 0.6$, $H = 3$, for (*a*) $S = 0.72$, (*b*) 0.43 and (*c*) 0 (non-stratified) NS predictions. Also shown are the SL result.

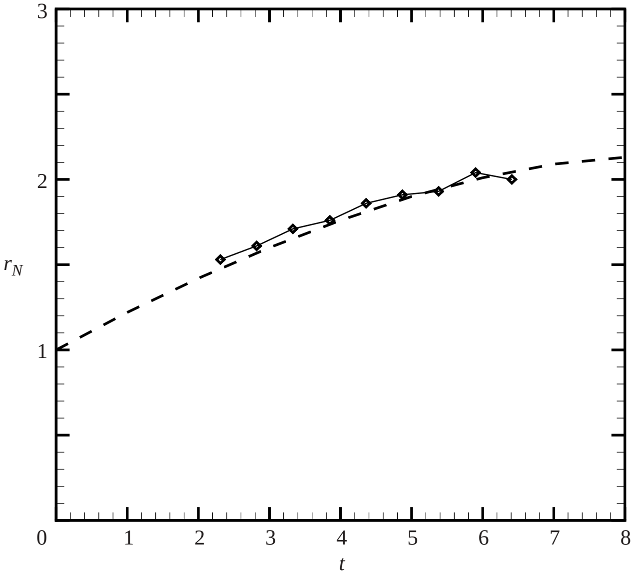

FIGURE 17. Radius of propagation as a function of time, experimental (solid line and symbols) and SW theory (dashed line) results. Here, $S = 1$, $H = 2.4$, $\mathscr{C} = 0.195$. The experimental data was scaled with $r_0 = 100.0\,\mathrm{cm}$, $h_0 = 33.0\,\mathrm{cm}$, $U = 25.63\,\mathrm{cm\,s^{-1}}$; also, $\Omega = 0.05\,\mathrm{s^{-1}}$ and $Re = 2.6 \times 10^5$.

or even suppressed by the Ekman layer at the bottom. In these cases the axisymmetric flow approximates well the mean real behaviour (except for the rim of the current where some azimuthal waves develop) (see Saunders 1973; Hallworth *et al.* 2001). Unfortunately, no relevant experiments have been published for a stratified ambient. Here, we briefly present a comparison with some preliminary results of a recent experiment performed at the large turntable (13 m diameter) Coriolis laboratory in Grenoble. The cylindrical lock had a radius $r_0 = 100\,\mathrm{cm}$ and typical height $h_0 = 30\,\mathrm{cm}$, and was filled with saltwater. The ambient saline was linearly stratified, of typical height 80 cm, and angular velocities $\Omega = 0.1$ and $0.05\,\mathrm{s^{-1}}$ were used. The dense fluid (current) was marked by fluorescein and tracer particles were mixed in. The experiment was started by lifting the lock (by motor) in about 2 s to a position slightly below the open surface of the ambient. Motion was marked by a vertical laser sheet. The detailed analysis of the data is still underway (Hallworth *et al.* 2004). The propagation results of one experiment are shown in figure 17, and compared with the SW prediction. The agreement is excellent, and this is very encouraging because, in the setting considered, the stratification was at the extreme $S = 1$. Here, the maximum radius is achieved in about 0.25 revolution of the system ($t \approx 8$).

4. Box models

Box models have been successfully used in the investigation of homogeneous and particle-driven currents in various configurations, as quick approximations to the features predicted by the SW theory and to determine the essential parameter influences. Here, we extend these models to the current in a stratified ambient, $0 \leqslant S \leqslant 1$, in both two-dimensional and axisymmetric (non-rotating) configurations. The main simplifying assumption is that the interface is a flat horizontal surface, $z = h_N(t)$.

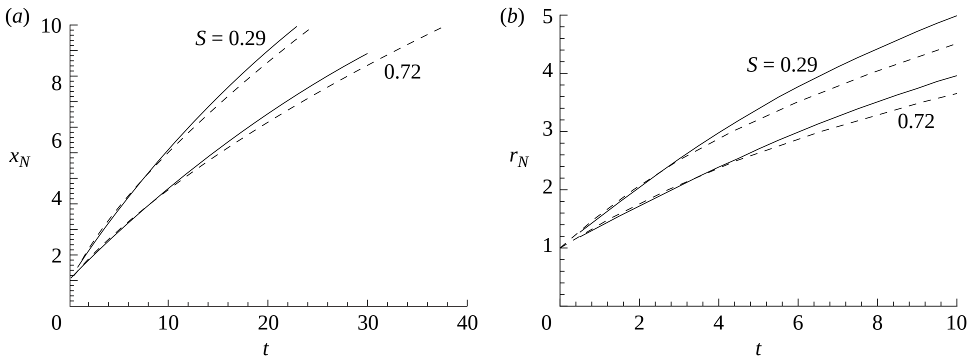

FIGURE 18. Propagation as a function of time, box-model (dashed line) and SW (solid line) predictions for $H = 3$ and two values of S, (a) two-dimensional and (b) axisymmetric.

Consider the two-dimensional case. Volume continuity now reads $h_N(t) = 1/x_N(t)$. Substituting this relationship into the nose propagation condition (2.17), it can be expressed as

$$\mathrm{d}t = \left\{ Fr\, h_N^{1/2} \times \left[1 - S\left(1 - \frac{1}{2}\frac{h_N}{H} \right) \right]^{1/2} \right\}^{-1} \mathrm{d}x, \tag{4.1}$$

with Fr given by (2.18), which can be integrated subject to $x_N(0) = 1$. Actually, t is a quadrature of $\mathrm{d}x/u_N(x)$ from 1 to $x_N(t)$ and the result is straightforward. The difference from the homogeneous case is contributed by the term in the square brackets in (4.1). This complicates the analytical solution (except for the $S = 1$ case), but is insignificant if numerical quadrature is used. Here, we used the trapezoidal method.

In the axisymmetric case, volume continuity now yields $h_N(t) = 1/r_N^2(t)$. A similar substitution provides t as a quadrature of $\mathrm{d}r/u_N(r)$ from 1 to $r_N(t)$.

A comparison for typical configurations between the box model and SW predictions of the propagation is presented in figure 18. The agreement is initially good, but eventually the box model results lag more and more behind the SW; this trend is more pronounced in the axisymmetric geometry. The box model captures well the influence of the stratification represented by the parameter S. We therefore conclude that the present model is a reliable extension of the similar box-model approximations for homogeneous currents, and can be used, with due care, as a first and quick estimate of the flow. The wave–nose interactions and rotation of the frame are not incorporated in this model.

Ungarish & Huppert (1999) showed that Coriolis effects can also be incorporated in box-model approximations, but in this case the horizontal interface must be replaced by an inclined one, i.e. the ‘box’ is a cone cylinder. This geometry allows the current to attain $h_N = 0$ at a finite radius of propagation. An extension for the stratified ambient seems feasible, but the details are not straightforward and this topic is not pursued here.

5. Concluding remarks

The shallow-water one-layer analysis for a constant-volume gravity current released instantaneously from behind a lock into a linearly stratified ambient, in both rectangular and axisymmetric (with and without rotation) geometries has been performed.

The SW equations of motion were integrated numerically by a Lax–Wendroff scheme. The results were compared to Navier–Stokes simulation and to laboratory experiments of Maxworthy *et al.* (2002) and Hallworth *et al.* (2004). A simplified box-model solution was also developed.

The one-layer SW formulation presented here is a versatile tool for the analysis of these problems. It seems to capture well the effects of stratification on the propagation of the gravity current, at least for the initial period of propagation. The solution by the Lax–Wendroff scheme is relatively easy to program, and the results are obtained in several CPU seconds. This is in contrast with the Navier–Stokes finite-difference solver which requires a considerable programming effort, and long computations and data processing on powerful computers.

The present shallow-water results do not reproduce the internal gravity waves and their possible interaction with the motion of the head. When the nose velocity is subcritical (i.e. smaller than that of the mode-one wave), this interaction will eventually hinder the propagation significantly below the SW predictions. However, we showed that this interaction occurs only after the nose has propagated two wavelengths from the lock, and that the SW results describe accurately the propagation in this period of motion. We developed simple yet fairly accurate formulae for predicting the current type (sub- or supercritical) for a given configuration, and the position where wave–nose interaction becomes important. The Navier–Stokes solver predicted correctly the head–wave interactions in the tested cases. Whether and how these internal gravity waves can be incorporated in the SW formulation is a topic for future work. Our idea is to regard the present SW current as an 'obstacle' encountered by the stratified media to analyse, and subsequently superpose, the resulting waves. The intrinsic time-dependent nature of this problem makes it a challenge.

Special attention was given to axisymmetric configurations, in particular in rotating frames, for which no previous results are available. Again, the SW theory provides satisfactory answers and insights. There are indications that the internal gravity waves are less important in this geometry because the current decays with the square of the radius and is already slow when the interaction occurs.

The effects of stratification on axisymmetric rotating gravity currents have been elucidated. This provides a useful extension of the classical Rossby adjustment axisymmetric problem to the stratified ambient circumstances. We showed that steady-state lens structures are feasible, as in the homogeneous case, and presented the pertinent approximate and numerical results that extend the classical $S=0$ results to $0 \leqslant S \leqslant 1$. For the maximal stratification $S=1$ case, the lens interface has a singularity of infinite slope at the rim, but the angular velocity remains regular. In this case, the aspect ratio is in agreement with that of a lens created by slow injection of non-rotating fluid at a neutral level (Gill 1981; Griffiths & Linden 1981; Hedstrom & Armi 1988). For the cases considered in our study, the energy of the lens is considerably smaller than in the initial state (i.e. the cylinder of dense fluid in the lock). The time-dependent rotating current released from behind a lock propagates by about 30% further than the radius predicted by the steady lens solution. This indicates some oscillatory adjustment motion and perhaps instabilities by which the initial energy excess is dissipated. The study of Stegner, Bouruet-Aubertot & Pichon (2004) for the homogeneous ambient provides some clues to the expected behaviour; the detailed investigation of the stratified counterpart is a topic for future work, for which the present results will provide the essential reference states. In general, as stratification increases, the relative importance of the Coriolis effects increases. This has been expressed by an effective dimensionless Coriolis parameter, $\mathscr{C}_e$, which seems to capture well the combined effects of rotation and stratification on the maximal radius of propagation. It is, however, remarkable that for any value of S, the maximum radius of propagation is attained in about 0.3 revolutions of the system.

The SW results for the axisymmetric and rotating currents are in good agreement with Navier–Stokes simulations and recent experimental data (preliminary results), which provides credence to the methodology and encouragement for future work. We hope that the progress in theory will stimulate more research, in particular experimental verifications, on this fascinating topic.

The research was supported by EPSRC and by the Technion VPR Fund – New-York Metropolitan Research Fund. We thank Professor T. Maxworthy for very useful discussions. Mrs T. Zemach and Dr M. Hallworth helped in the preparation of figure 17; the laboratory work was supported by the EEC contract 'Transitional Access to Major Research Infrastructures' HPRI-1999-CT-00006. The manuscript was finalized while H. E. H held a Gledder Fellowship at the University of Western Australia. He thanks Jorg Imberger and the members of Center for Water Resources for their kind hospitality. The laboratory work was supported by the EEC contract 'Transnational Access to Major Research Infrastructures' HPRI-1999-CT-00006.

Appendix. Navier–Stokes numerical simulation (NS) approach

Here we present some details of the NS formulation and finite-difference solution. We focus attention on the more complex axially symmetric rotating configuration; the two-dimensional case follows by a straightforward modification.

We introduce the dimensionless density function $\phi(\mathbf{r}, t)$ defined by

$$\rho(\boldsymbol{r}, t) = \rho_o[1 + \epsilon\phi(\boldsymbol{r}, t)], \tag{A 1}$$

where, again, ρ_o is the *dimensional* density of the ambient at the top open surface. We expect $0 \leqslant \phi \leqslant 1$, with $\phi = 1$ in the 'pure' dense fluid domain. In the ambient, ϕ varies between 0 and S.

The dimensionless governing equations are as follows.

(i) Continuity of volume

$$\nabla \cdot \boldsymbol{v} = 0. \tag{A 2}$$

(ii) Momentum balance in the radial (horizontal), azimuthal and axial (vertical) directions

$$\frac{\mathrm{D}u}{\mathrm{D}t} - 2\mathscr{C}^2 v - \mathscr{C}^2\frac{v^2}{r} = \frac{1}{1+\epsilon\phi}\left[-\frac{\partial p}{\partial r} + \phi\epsilon\mathscr{C}^2 r + \frac{1}{Re}\nabla_c^2 u\right], \tag{A 3}$$

$$\frac{\mathrm{D}v}{\mathrm{D}t} + \frac{uv}{r} + 2u = \frac{1}{1+\epsilon\phi}\left[\frac{1}{Re}\nabla_c^2 v\right], \tag{A 4}$$

$$\left(\frac{h_0}{r_0}\right)^2\frac{\mathrm{D}w}{\mathrm{D}t} = \frac{1}{1+\epsilon\phi}\left[-\frac{\partial p}{\partial z} - \phi + \frac{1}{Re}\left(\frac{h_0}{r_0}\right)^2\nabla^2 w\right]. \tag{A 5}$$

(iii) Dense component transport

$$\frac{\mathrm{D}\phi}{\mathrm{D}t} = \mathscr{D}\nabla^2\phi, \tag{A 6}$$

where we have used the notations

$$\nabla^2 f = \frac{1}{r}\frac{\partial}{\partial r}r\frac{\partial f}{\partial r} + \left(\frac{h_0}{r_0}\right)^{-2}\frac{\partial^2 f}{\partial z^2}, \quad \nabla_c^2 f = \nabla^2 f - \frac{f}{r^2}. \tag{A 7}$$

The relevant dimensionless parameters in these equation, in addition to the reduced density difference ϵ and the initial aspect ratio h_0/r_0, are the Coriolis to inertia ratio parameter $\mathscr{C}$, see (3.4), the Reynolds number

$$Re = (g' h_0)^{1/2} r_0 \rho_o/\mu, \tag{A 8}$$

and the dimensionless diffusion coefficient $\mathscr{D} = 1/Pe = 1/(\sigma Re)$, where Pe and σ are the Péclet and Schmidt numbers, and μ is the dynamic viscosity, assumed constant in the flow field.

We are interested in flows with large values of Re, moderately small $\mathscr{C}$, small ϵ and very small $\mathscr{D}$. The typical physical value of $\mathscr{D}$ is negligibly small (recall that $\sigma \gg 1$ for saline solutions in water), but here a non-vanishing $\mathscr{D}$ is used as an artificial diffusion coefficient for numerical smoothing.

The Ekman number can be defined in terms of the previous parameters as

$$\mathscr{E} = \frac{\mu}{\Omega h_0^2 \rho_o} = \left[\left(\frac{h_0}{r_0} \right)^2 \mathscr{C} Re \right]^{-1} \tag{A 9}$$

and is assumed small; $\mathscr{E}^{1/2}$ is the typical (dimensionless) thickness of the rotational horizontal viscous layers which develop after about one revolution of the system.

The parameter (h_0/r_0) represents the 'shallowness' of the current, and is assumed small. In the axially symmetric lock-release problem simulated here, two more geometric parameters appear: the initial ratio of the total height of the ambient fluid to the height of the dense fluid in the lock (or the dimensionless total height of the fluids), H, and the initial length ratio (or the dimensionless radius of the container), r_w. The former may assume various values (but evidently must be at least 1, and typically is large), and the latter is assumed sufficiently large not to interfere with the motion of the current for the time period of interest.

The initial conditions at $t = 0$ are

$$\boldsymbol{v} = 0 \quad (0 \leqslant r \leqslant r_w,\ 0 \leqslant z \leqslant H), \tag{A 10}$$

$$\phi = \begin{cases} 1 & (0 \leqslant r \leqslant 1, \quad 0 \leqslant z \leqslant 1), \\ S(1 - z/H) & \text{elsewhere.} \end{cases} \tag{A 11}$$

The boundary conditions for $t \geqslant 0$ are

$$\boldsymbol{v} = 0 \ \text{ (on the bottom and sidewalls)}, \tag{A 12}$$

$$w = 0 \ \text{ and no shear } \quad (z = H), \tag{A 13}$$

$$u = 0 \ \text{ and regularity } \quad (r = 0), \tag{A 14}$$

and

$$\hat{n} \cdot \nabla \phi = 0 \quad \text{(on all boundaries).} \tag{A 15}$$

These conditions contain some simplifications, in particular (A 13) which is the frictionless 'rigid lid' approximation for the free surface. The initial interfaces (between the ambient and dense fluids, and also the free surface of the ambient fluid) deviate from the horizontal by an amount $\epsilon \mathscr{C}^2 r^2/2$. The free surface will also have an additional $O(\epsilon)$ deformation during the flow. The neglect of these departures from the horizontal is justified for the small values of ϵ and $\mathscr{C}^2$ used in this investigation. In addition, we assume that the lock is removed instantaneously and without any perturbation to the fluid. (In real situations, such as laboratory experiments, the lock

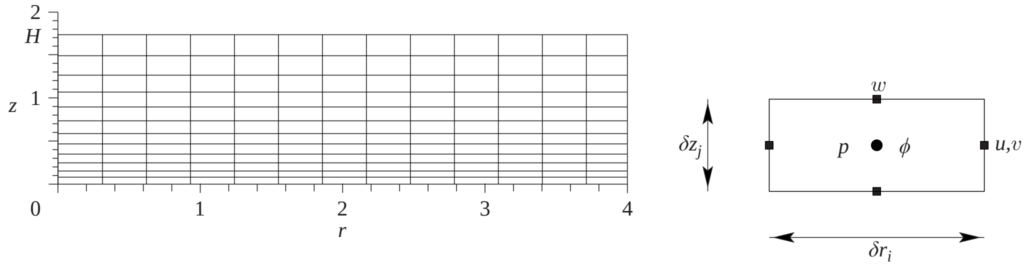

FIGURE 19. Sketch of numerical grid ($r_w = 4, H = 1.75$), and the details of one cell. The centre of the computational cell is denoted by (i, j), corresponding to the position r_i, z_j, $(1 \leqslant i \leqslant il,\ 1 \leqslant j \leqslant jl)$.

lifting is expected to introduce a small delay in the initial motion, which is a slight source of discrepancy between theory and measurements.)

The foregoing system of equations and boundary conditions, subject to the axial-symmetry assumption, is solved by a time-marching-finite-difference discretization method. The details are described in Hallworth *et al.* (2001).

Briefly, the method is based on forward-time discretization of the velocity components, with implicit Coriolis and pressure terms. The continuity equation for the new velocity field yields an elliptic equation for the new pressure field.

The spatial discretization is performed on a staggered grid with il radial intervals and jl axial intervals, as sketched in figure 19. The variables p and ϕ are defined at the mid-cell position denoted (i, j); u and v are both defined at the positions $(i \pm 1/2, j)$ (to allow straightforward implementation of the Coriolis coupling) and w is defined at $(i, j \pm 1/2)$. Both the r and z grid coordinates are stretched by the simple mapping functions $r(R)$ and $z(Z)$. The grids $R_i = (i + 1/2)\delta R$ and $Z_j = (j + 1/2)\delta Z$ are uniform in the domain $(0 \leqslant R \leqslant r_w,\ 0 \leqslant Z \leqslant H)$ with intervals $\delta R = r_w/il$, and $\delta Z = H/jl$. The truncation error is $O(\delta R^2 + \delta Z^2)$. Dummy cells were added for easy implementation of boundary conditions. An illustration of the finite-difference approximation approach is

$$\left(\frac{1}{r}\frac{\partial}{\partial r} r \frac{1}{1+\epsilon\phi}\frac{\partial p}{\partial r}\right)_{r_i, z_j} \approx \frac{1}{r_i}\frac{1}{r_i'\delta R}\left(Y_{i+1/2,j} - Y_{i-1/2,j}\right), \tag{A 16}$$

where

$$Y_{i+1/2,j} = r_{i+1/2}\frac{1}{1+\epsilon\phi_{i+1/2,j}}\frac{1}{r_{i+1/2}'\delta R}(p_{i+1,j} - p_{i,j}) \tag{A 17}$$

and r_i' is the derivative of $r(R)$ at R_i (substituting $i - 1$ in place of i yields $Y_{i-1/2,j}$).

This method of central differences was employed for all terms, except for the advection terms in the transport equation for ϕ, (A 6). The interface between the pure and the dense fluids is represented by a sharp gradient in ϕ which may causes strong oscillations in numerical finite-difference schemes. To avoid this spurious effect, in the solution of (A 6) we implemented MacCormack's explicit method, see Anderson, Tannehill & Pletcher (1984), i.e. we used at each time step a predictor–corrector relationship which combines forward and backward differences of the advection terms in two half-steps. Comparisons of computed results confirmed the smoothing effect of this approach.

The combination of the foregoing time and space discretization are the core of the computer code used in this work. For each time step, the discretized form of the

Poisson equation for the 'new' pressure variables $p^{+}_{i,j}, 1 \leqslant i \leqslant il, 1 \leqslant j \leqslant jl$ must be solved. This yields, after the implementation of the boundary conditions, a block tri-diagonal linear system which was solved by a bi-conjugate gradient iterative algorithm, see Press *et al.* (1992). The computations use real-8 variables. The typical grid has $il = 320$ constant radial intervals and $jl = 200$ slightly stretched axial intervals and the typical time step was $\delta t = 10^{-3}$.

The choice of the numerical grid parameters was motivated by the compromise between accuracy and computational limitations. Essentially, the mesh intervals are considerably smaller than the expected typical corresponding geometrical dimensions of the simulated current (e.g. the length of the 'head', the average thickness, and even the Ekman-layer thickness (estimated as $3\mathscr{E}^{1/2}$). The outer wall is far enough from the current to avoid perturbations from the reflected mode-one internal gravity wave during the simulated time interval. We therefore expect that the numerical results provide an acceptable simulation of an observable gravity-current process, at least during the initial period. Eventually, when the current becomes thin (say, of about 10 axial intervals) and the interface is very irregular, the numerical errors may become significant and even dominant.

The two-dimensional version of the foregoing formulation in a rectangular non-rotating x,z-coordinate system is obtained as follows: (a) set $v \equiv 0$, $\mathscr{C} = 0$, and replace r with x; (b) delete the curvature terms; and (c) change the regularity boundary condition on the axis, (A 14), to $w = 0$. This case was presented in HU (the scaling here is slightly different).

REFERENCES

Anderson, D. A., Tannehill, J. C. & Pletcher, R. M. 1984 *Computational Fluid Mechanics and Heat Transfer*. Hemisphere, NY.

Baines, P. G. 1995 *Topographic Effects in Stratified Flows*. Cambridge University Press.

Benjamin, T. B. 1968 Gravity currents and related phenomena. *J. Fluid Mech.* **31**, 209–248.

Bonnecaze, R. T., Hallworth, M. A., Huppert, H. E. & Lister, J. R. 1995 Axisymmetric particle-driven gravity currents. *J. Fluid Mech.* **294**, 93–121.

Bonnecaze, R. T., Huppert, H. E. & Lister, J. R. 1993 Particle-driven gravity currents. *J. Fluid Mech.* **250**, 339–369.

Csanady, G. T. 1979 The birth and death of a warm core ring. *J. Geophys. Res.* **84**, 777–780.

Gill, A. E. 1981 Homogeneous intrusion in a rotating stratified fluid. *J. Fluid Mech.* **103**, 275–295.

Griffiths, R. W. & Linden, P. 1981 The stability of vortices in a rotating, stratified fluid. *J. Fluid Mech.* **105**, 283–316.

Hallworth, M. A., Huppert, H., Ungarish, M. & Zemach, T. 2004 Axisymmetric gravity currents in a atratified rotating system: experimental and numerical investigations. *In preparation*.

Hallworth, M. A., Huppert, H. E. & Ungarish, M. 2001 Axisymmetric gravity currents in a rotating system: experimental and numerical investigations. *J. Fluid Mech.* **447**, 1–29.

Hedstrom, K. & Armi, L. 1988 An experimental study of homogeneous lenses in a stratified rotating fluid. *J. Fluid Mech.* **191**, 535–556.

Hogg, A. J., Hallworth, M. A. & Huppert, H. E. 1999 Reversing buoyancy of particle-driven gravity currents. *Phys. Fluids* **11**, 2891–2900.

Huppert, H. E. 1998 Quantitative modelling of granular suspension flow. *Phil. Trans. R. Soc. Lond.* A **356**, 2471–2496.

Huppert, H. E. 2000 Geological fluid mechanics. In *Perspectives in Fluid Dynamics: A Collective Introduction to Current Research* (ed. G. K. Batchelor, H. K. Moffatt & M. G. Worster), pp. 447–506. Cambridge University Press.

Huppert, H. E. & Simpson, J. E. 1980 The slumping of gravity currents. *J. Fluid Mech.* **99**, 785–799.

Klemp, J. B., Rotunno, R. & Skamarock, W. C. 1994 On the dynamics of gravity currents in a channel. *J. Fluid Mech.* **269**, 169–198.

Manasseh, R., Ching, C.-Y. & Fernando, H. J. S. 1998 The transition from density-driven to wave-dominated isolated flows. *J. Fluid Mech.* **361**, 253–274.

Maxworthy, T., Leilich, J. Simpson, J. E. & Meiburg, E. H. 2002 The propagation of gravity currents in a linearly stratified fluid. *J. Fluid Mech.* **453**, 371–394.

Morton, K. W. & Mayers, D. F. 1994 *Numerical Solutions of Partial Differential Equations.* Cambridge University Press.

Press, W. H., Teukolski, S. A., Vetterling, W. T. & Flannery, B. P. 1992 *Numerical Recipes in Fortran.* Cambridge University Press.

Saunders, P. M. 1973 The instability of a baroclinic vortex. *J. Phys. Ocean.* **3**, 61–65.

Simpson, J. E. 1997 *Gravity Currents in the Environment and the Laboratory.* Cambridge University Press.

Stegner, A., Bouruet-Aubertot, P. & Pichon, T. 2004 Nonlinear adjustment of density fronts. Part 1. The Rossby scenario and the experimental reality. *J. Fluid Mech.* **502**, 335–360.

Ungarish, M. 2004 Dam-break release of a gravity current in a stratified ambient. *Eur. J. Mech.* B/*Fluids* (submitted).

Ungarish, M. & Huppert, H. E. 1998 The effects of rotation on axisymmetric particle-driven gravity currents. *J. Fluid Mech.* **362**, 17–51.

Ungarish, M. & Huppert, H. E. 1999 Simple models of Coriolis-influenced axisymmetric particle-driven gravity currents. *Intl J. Multiphase Flow* **25**, 715–737.

Ungarish, M. & Huppert, H. E. 2002 On gravity currents propagating at the base of a stratified ambient. *J. Fluid Mech.* **458**, 283–307.

Ungarish, M. & Zemach, T. 2003 On axisymmetric rotating gravity currents: two-layer shallow-water and numerical solutions. *J. Fluid Mech.* **481**, 37–66.

Verzicco, R., Lalli, F. & Campana, E. 1997 Dynamics of baroclinic vortices in a rotating, stratified fluid: a numerical study. *Phys. Fluids* **9**, 419–432.